Building a Smart EM Environment - AI-Enhanced Aperiodic Micro-Scale Design of Passive EM Skins

Giacomo Oliveri, *Senior Member, IEEE*, Francesco Zardi, Paolo Rocca, *Senior Member, IEEE*, Marco Salucci, *Senior Member, IEEE*, and Andrea Massa, *Fellow, IEEE*

Abstract— An innovative process for the design of static passive smart skins (SPSSs) is proposed to take into account, within the synthesis, the electromagnetic (EM) interactions due to their finite (macrolevel) size and aperiodic (microscale) layouts. Such an approach leverages the combination of an inverse source (IS) formulation, to define the SPSS surface currents, and of an instance of the system-by-design paradigm, to synthesize the unit cell (UC) descriptors suitable for supporting these currents. As for this latter step, an enhanced artificial intelligence (IA)-based digital twin (DT) is built to efficiently and reliably predict the relationships among the UCs and the nonuniform coupling effects arising when the UCs are irregularly assembled to build the corresponding SPSS. Toward this end and unlike state-of-the-art approaches, an aperiodic finite small-scale model of the SPSS is derived to generate the training database for the DT implementation. A set of representative numerical experiments, dealing with different radiation objectives and smart skin apertures, is reported to assess the reliability of the conceived design process and illustrate the radiation features of the resulting layouts, validated with accurate full-wave simulations, as well.

Index Terms— Electromagnetic (EM) holography, iterative projection method, metasurfaces, metamaterials, next-generation communications, smart skins, system-by-design.

Giacomo Oliveri, Francesco Zardi, and Marco Salucci are with the ELEDIA Research Center (ELEDIA@UniTN), Department of Civil, Environmental, and Mechanical Engineering (DICAM), University of Trento, 38123 Trento, Italy (e-mail: giacomo.oliveri@unitn.it; francesco.zardi@unitn.it; marco.salucci@unitn.it).

Paolo Rocca is with the ELEDIA Research Center (ELEDIA@UniTN), Department of Civil, Environmental, and Mechanical Engineering (DICAM), University of Trento, 38123 Trento, Italy, and also with the ELEDIA Research Center (ELEDIA@XIDIAN-Xidian University), Xi'an, Shaanxi 710071, China (e-mail: paolo.rocca@unitn.it).

Andrea Massa is with the ELEDIA Research Center (ELEDIA@UESTC-UESTC), School of Electronic Engineering, Chengdu 611731, China, also with the ELEDIA Research Center (ELEDIA@UniTN), Department of Civil, Environmental, and Mechanical Engineering (DICAM), University of Trento, 38123 Trento, Italy, and also with the ELEDIA Research Center (ELEDIA@TSINGHUA-Tsinghua University), Beijing, Haidian 100084, China (e-mail: andrea.massa@unitn.it).

Color versions of one or more figures in this article are available at https://doi.org/10.1109/TAP.2022.3151354.

Digital Object Identifier 10.1109/TAP.2022.3151354

I. INTRODUCTION AND RATIONALE

THE smart electromagnetic environment (SEE) vision is at the core of a revolutionary approach currently emerging in the design and the implementation of next-generation wireless cellular systems [1]–[9]. The academic and industrial interests in such a transformative paradigm are motivated by the unprecedented SEE potentialities in terms of blind spot mitigation, coverage improvement, and electromagnetic (EM) propagation control enabled by the opportunistic exploitation of the wireless power already available within the propagation scenario [2], [7], [10]. Moreover, a minimization of the power consumption of the wireless infrastructure and a reduction of the overall EM pollution are also assured due to the improved wireless efficiency without the need of installing new base stations [1]–[9].

Within this framework, static passive smart skins (SPSSs) have been conceived to guarantee the minimum impact in terms of fabrication, installation, maintenance, costs, and power consumption [7], [11]. An SPSS is an artificial passive structure that "manipulates" (i.e., reflection/focusing) the incident power radiated by one or more base stations toward the desired coverage region [7], [11]. Toward this end, SPSS implementations usually leverage on the capabilities of passive modulated thin metasurfaces to control the EM reflection due to their microscale physical structure [11], [12], rather than using active elements, such as diodes, varactors, phase shifters, or amplifiers [12], [13]. Therefore, there are no running costs after the installation and no electrical nor processing power is required to operate, thus making SPSSs particularly attractive for an inexpensive and fast deployment in large-scale scenarios [11]. Indeed, despite the technological simplicity and the relatively low-cost implementation, SPSSs can yield an excellent EM propagation control as already evidenced in several different "surface EM" applications, including lenses, beam splitters, wave polarizers, and reflect/transmit arrays [12].

However, the design of practically feasible SPSSs in SEE must fulfill very strict and contrasting requirements often not occurring in standard surface EM problems [11]. On the one hand, the use of multilayer/complex shapes or expensive materials in the unit cells (UCs) of the SPSS is prevented for costs and weight reasons. On the other hand, there is a need for high performance in terms of both pattern shaping and independence on the polarization of the incident field. To address such challenges, a customization of the system-by-design (SbD) paradigm [4], [14]–[16] has been recently proposed in [11]. By formulating the complex multiscale EM design problem at hand according to the generalized sheet

transition condition (GSTC) technique [12], [17]–[19], the approach in [11] combines a phase-only inverse source (IS) method to find the reference surface currents induced on the structure with the iterative projection technique (IPT) [20] together with an integration between a global optimization algorithm and a UC digital twin (UC-DT) to determine the descriptors of the SPSS that supports the IPT-synthesized currents [11]. In order to significantly speed up the generation of the training set for learning the UC-DT, the UC response is modeled by assuming local periodicity conditions [11] as usually done in the literature on surface EMs [12], [14], [15], [21]–[23]. Unfortunately, the aperiodicity and the edge effects of finite layouts introduce a degree of approximation that is very difficult to compensate in the final full-scale SPSS. Such an issue is particularly challenging when dealing with electrically large apertures since the optimization of the finite layout becomes computationally unmanageable. This article then proposes an innovative approach to face these challenges by extending and generalizing the method conceived in [11]. More in detail, the SPSS synthesis is still split into two steps, but, unlike [11], the UC-DT of the second step (i.e., the definition of the microscale descriptors of the UC so that the arising modulated metasurface supports the reference currents synthesized at the first IS step) avoids periodic assumptions, and it predicts the behavior of each UC by taking into account a finite set of neighboring cells and different locations of the same UC within the so-called small-scale model. The local susceptibility tensor of this latter is then computed with a full-wave commercial solver [24] and afterward exploited in an artificial intelligence (AI)-driven learning process to build the "local UC-DT."

To the best of our knowledge, the main innovative contributions of this work include: 1) the introduction of a local UC-DT for the reliable design of effective large-scale SPSSs by taking into account the local aperiodicity and the edge effects of the finite structure; 2) an efficient integration of such a DT within the SbD-based SPSS synthesis process; and 3) the full-wave modeling/simulation of the arising SPSS layouts to carefully assess their performance in realistic operative scenarios.

The outline of the article is given as follows. The design problem at hand is formulated in Section II, while the proposed synthesis process is detailed in Section III. A selected set of numerical examples is reported, and the synthesis outcomes are assessed with full-wave simulations in realistic operative conditions (see Section IV). Finally, some conclusions follow (see Section V).

II. SPSS PROBLEM FORMULATION

Let us consider the SEE scenario in Fig. 1, where an SPSS of $P \times Q$ UCs, arranged on the xy-plane according to a regular lattice with spacings Δx and Δy, is illuminated by a plane wave of TE/TM complex components $E_{TE}^{inc}/E_{TM}^{inc}$ that impinges from the angular direction $(\theta^{inc}, \varphi^{inc})$. The design of the SPSS can be stated as follows.

SPSS Design Problem: Given $(\theta^{inc}, \varphi^{inc})$, E_{TE}^{inc}, and E_{TM}^{inc}, find $\mathbf{G}$ such that $\mathcal{O}[\mathbf{F}(\mathbf{r}; \mathbf{G})]$ is minimized,
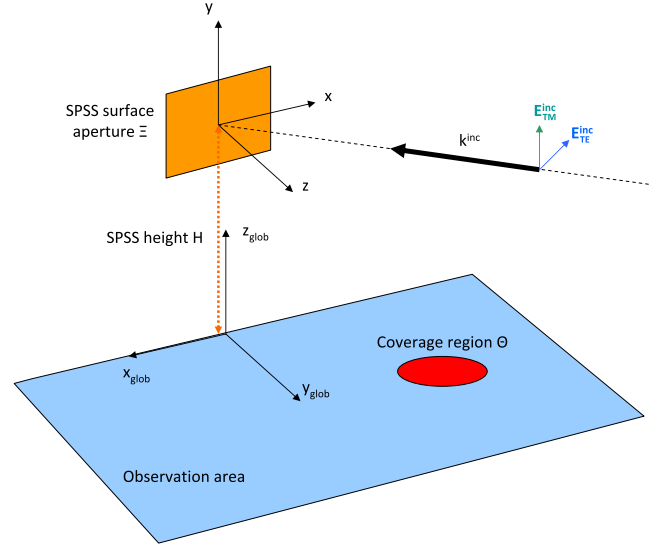

Fig. 1. Problem geometry. Sketch of the smart EM environment (SEE) scenario.

where $\mathbf{G}$ is the vector of the descriptors of the SPSS (i.e., the set of $P \times Q$ UCs) ($\mathbf{G} \triangleq \{\mathbf{g}_{pq}; \ p = 1, \ldots, P, \ q = 1, \ldots, Q\}$), whose D-sized (p, q)th ($p = 1, \ldots, P; \ q = 1, \ldots, Q$) entry, $\mathbf{g}_{pq} \triangleq \{g_{pq}^{(d)}; \ d = 1, \ldots, D\}$, lists the geometrical/physical microscale parameters of the corresponding UC. Moreover, $\mathbf{F}(\mathbf{r}; \mathbf{G})$ is the electric field reflected by the SPSS in a far-field point with local coordinates $\mathbf{r} = (x, y, z)$, while $\mathcal{O}[\mathbf{F}(\mathbf{r}; \mathbf{G})]$ is the implicit form of the macroscale radiation objectives set on the far-field pattern, $\mathbf{F}(\mathbf{r}; \mathbf{G})$, whose explicit expression is defined case-by-case according to the specific applicative context.

Regardless of $\mathcal{O}[\mathbf{F}(\mathbf{r})]$, the solution of the SPSS design problem requires a reliable approach to compute $\mathbf{F}(\mathbf{r}; \mathbf{G})$ starting from $(\theta^{inc}, \varphi^{inc})$, E_{TE}^{inc}, E_{TM}^{inc}, and $\mathbf{G}$. In principle, such a task may be accomplished by modeling the entire SPSS layout and computing the solution with a full-wave numerical solver. This strategy is practically prevented because of the unfeasible computational costs related to the need of performing an expensive computation of $\mathbf{F}(\mathbf{r}; \mathbf{G})$ for each guess configuration of $\mathbf{G}$. On the other hand, it is worth pointing out that careful modeling of the SPSS allows the designer to exploit the intrinsic nonuniqueness of the underlying IS problem (i.e., the deduction of the SPSS surface currents from the radiated far-field pattern) that gives greater flexibility in the synthesis of wave manipulation devices [25].

By taking into account these considerations, a different approach is adopted by exploiting the concept of equivalent surface currents within the GSTC framework [11], [12]. More in detail, the far-field pattern reflected by the SPSS is defined as $\mathbf{F}(\mathbf{r}; \mathbf{G}) \triangleq \mathcal{L}[\mathbf{J}^{tot}(\mathbf{r}; \mathbf{G})]$, $\mathcal{L}[\cdot]$ being the far-field Green's operator, and it computed as [11], [26]

$$\mathbf{F}(\mathbf{r}; \mathbf{G}) = \frac{jk_0}{4\pi} \frac{\exp(-jk_0|\mathbf{r}|)}{|\mathbf{r}|}$$
$$\times \int_\Xi \left\{ \mathbf{J}^{tot}(\widetilde{\mathbf{r}}; \mathbf{G}) \exp(jk_0\hat{\mathbf{r}} \cdot \widetilde{\mathbf{r}}) \right\} d\widetilde{\mathbf{r}} \quad (1)$$

where $\hat{\mathbf{r}} \triangleq (\mathbf{r}/|\mathbf{r}|)$, k_0 is the free-space wavenumber, and Ξ is the SPSS surface aperture, while $\mathbf{J}^{tot}$ is the surface equivalent

source induced on Ξ () and computed as the superposition of the electric, $\mathbf{J}^e$, and the magnetic, $\mathbf{J}^m$, effective current components

$$\mathbf{J}^{tot}(\mathbf{r}; \mathbf{G}) = \widehat{\mathbf{r}} \times \left[\eta_0 \widehat{\mathbf{r}} \times \mathbf{J}^e(\mathbf{r}; \mathbf{G}) + \mathbf{J}^m(\mathbf{r}; \mathbf{G}) \right] \quad (2)$$

η_0 being the free-space impedance ($\eta_0 \triangleq \sqrt{(\mu_0/\varepsilon_0)}$, and ε_0 and μ_0 being the free-space permittivity and permeability, respectively).

According to the GSTC technique [12], [19], the current components $\mathbf{J}^e$ and $\mathbf{J}^m$ are functions of the electric, $\mathbf{S}^e(\mathbf{r}; \mathbf{G})$, and magnetic, $\mathbf{S}^m(\mathbf{r}; \mathbf{G})$, polarization surface densities so that $\mathbf{J}^e(\mathbf{r}; \mathbf{G}) = j\omega \mathbf{S}_t^e(\mathbf{r}; \mathbf{G}) - \widehat{\mathbf{n}} \times \nabla_t S_n^m(\mathbf{r}; \mathbf{G})$ and $\mathbf{J}^m(\mathbf{r}; \mathbf{G}) = j\omega\mu_0 \mathbf{S}_t^m(\mathbf{r}; \mathbf{G}) + (1/\varepsilon_0)\widehat{\mathbf{n}} \times \nabla_t S_n^e(\mathbf{r}; \mathbf{G})$, $\widehat{\mathbf{n}}$ being the normal to the smart skin surface Ξ, while $\mathbf{S}_t^{e/m}(\mathbf{r}; \mathbf{G}) \triangleq \mathbf{S}^{e/m}(\mathbf{r}; \mathbf{G}) \times \widehat{\mathbf{n}}$ and $S_n^{e/m}(\mathbf{r}; \mathbf{G}) \triangleq \mathbf{S}^{e/m}(\mathbf{r}; \mathbf{G}) \cdot \widehat{\mathbf{n}}$. Moreover, for (sufficiently) symmetric UCs, $\mathbf{S}^e$ and $\mathbf{S}^m$ are given by

$$\mathbf{S}^e(\mathbf{r}; \mathbf{G}) = \sum_{p=1}^{P} \sum_{q=1}^{Q} \left[\varepsilon_0 \overline{\overline{\psi}}_{pq}^e(\mathbf{G}) \cdot \mathbf{E}_{pq}^{ave}(\mathbf{G}) \right] \Psi^{pq}(\mathbf{r}) \quad (3)$$

and

$$\mathbf{S}^m(\mathbf{r}; \mathbf{G}) = \sum_{p=1}^{P} \sum_{q=1}^{Q} \left[\overline{\overline{\psi}}_{pq}^m(\mathbf{G}) \cdot \mathbf{H}_{pq}^{ave}(\mathbf{G}) \right] \Psi^{pq}(\mathbf{r}) \quad (4)$$

where $\Psi^{pq}(\mathbf{r}) \triangleq \{1 \, if \, \mathbf{r} \in \Xi_{pq}, \, 0 \, if \, \mathbf{r} \notin \Xi_{pq}\}$, Ξ_{pq} being the support of the (p, q)th ($p = 1, \ldots, P; \, q = 1, \ldots, Q$) UC so that $\Xi = \sum_{p=1}^{P} \sum_{q=1}^{Q} \Xi_{pq}$.

The computation of (3) and (4) only requires to determine the electric/magnetic local surface susceptibility diagonal tensors $\overline{\overline{\psi}}_{pq}^{e/m}(\mathbf{G})$ of the (p, q)th ($p = 1, \ldots, P; \, q = 1, \ldots, Q$) UC since the surface averaged fields $\mathbf{\Phi}_{pq}^{ave}(\mathbf{G})$ ($\mathbf{\Phi} = \{\mathbf{E}, \mathbf{H}\}$) are given by [11], [12]

$$\mathbf{\Phi}_{pq}^{ave}(\mathbf{G}) \triangleq \frac{1}{2 \times \Delta x \times \Delta y} \int_{\Xi_{pq}} \left\{ \mathbf{1} + \overline{\overline{R}} \left[\overline{\overline{\psi}}_{pq}^{e/m}(\mathbf{G}) \right] \right\}$$
$$\cdot \mathbf{\Phi}^{inc}(\mathbf{r}) d\mathbf{r} \quad \mathbf{\Phi} = \{\mathbf{E}, \mathbf{H}\} \quad (5)$$

where the incident electric

$$\mathbf{E}^{inc}(\mathbf{r}) \triangleq \left(E_{TE}^{inc} \widehat{\mathbf{e}}_{TE} + E_{TM}^{inc} \widehat{\mathbf{e}}_{TM} \right) \exp\left(-j\mathbf{k}^{inc} \cdot \mathbf{r} \right) \quad (6)$$

and magnetic

$$\mathbf{H}^{inc}(\mathbf{r}) \triangleq \frac{1}{\eta_0 k_0} \mathbf{k}^{inc} \times \mathbf{E}^{inc}(\mathbf{r}) \quad (7)$$

fields are known quantities, $\mathbf{k}^{inc}$ and $\widehat{\mathbf{e}}_{TE/TM}$ being the incident wave vector ($\mathbf{k}^{inc} \triangleq - k_0 \, [\sin(\theta^{inc})\cos(\varphi^{inc})\widehat{\mathbf{x}} + \sin(\theta^{inc})\sin(\varphi^{inc})\widehat{\mathbf{y}} + \cos(\theta^{inc})\widehat{\mathbf{z}}]$) and the TE/TM mode unit vectors ($\widehat{\mathbf{e}}_{TE} = (\mathbf{k}^{inc} \times \widehat{\mathbf{n}}/|\mathbf{k}^{inc} \times \widehat{\mathbf{n}}|)$; $\widehat{\mathbf{e}}_{TM} = (\widehat{\mathbf{e}}_{TE} \times \mathbf{k}^{inc}/|\widehat{\mathbf{e}}_{TE} \times \mathbf{k}^{inc}|)$), respectively, while $\mathbf{1}$ is a diagonal unitary tensor, and $\overline{\overline{R}}[\overline{\overline{\psi}}_{pq}^{e/m}(\mathbf{G})] \triangleq R^{TE,TE}[\overline{\overline{\psi}}_{pq}^{e/m}(\mathbf{G})] \widehat{\mathbf{e}}_{TE}\widehat{\mathbf{e}}_{TE} + R^{TE,TM}[\overline{\overline{\psi}}_{pq}^{e/m}(\mathbf{G})] \widehat{\mathbf{e}}_{TE}\widehat{\mathbf{e}}_{TM} + R^{TM,TE}[\overline{\overline{\psi}}_{pq}^{e/m}(\mathbf{G})] \widehat{\mathbf{e}}_{TM}\widehat{\mathbf{e}}_{TE} + R^{TM,TM}[\overline{\overline{\psi}}_{pq}^{e/m}(\mathbf{G})] \widehat{\mathbf{e}}_{TM}\widehat{\mathbf{e}}_{TM}$ is the local reflection tensor, which can be derived from $\overline{\overline{\psi}}_{pq}^{e/m}(\mathbf{G})$ [12].

It is worthwhile to point out that here, unlike [11], the electric/magnetic local surface susceptibility diagonal tensors $\overline{\overline{\psi}}_{pq}^{e/m}$ of the (p, q)th ($p = 1, \ldots, P; \, q = 1, \ldots, Q$) UC depend on the whole finite structure of the SPSS [i.e., $\overline{\overline{\psi}}_{pq}^{e/m} = \overline{\overline{\psi}}_{pq}^{e/m}(\mathbf{G})$] instead of on the D descriptors of the same (p, q)th UC [i.e., $\overline{\overline{\psi}}_{pq}^{e/m} = \overline{\overline{\psi}}_{pq}^{e/m}(\mathbf{g}_{pq})$]. The interested reader should also notice that such an IS-based formulation of the SPSS problem [i.e., (1)–(3) and (4) with the intermediate step (2) for the computation of the induced surface current, $\mathbf{J}^{tot}(\mathbf{r}; \mathbf{G})$], allows one to exploit the multiplicity of the induced currents [25] to identify the most proper (i.e., physically admissible and easy-to-build) SPSS layout for the scenario/objectives at hand. On the other hand, it is evident the multiscale nature of the SPSS synthesis problem since the fulfillment of the macroscale objectives, $\mathcal{O}[\mathbf{F}(\mathbf{r}; \mathbf{G})]$, is obtained by optimizing the microscale descriptors of the UCs, $\mathbf{G}$. Last but not least, the design of an SPSS intrinsically features complexity and high-dimensionality since the number of degrees-of-freedom (DoFs), $\mathcal{N} \triangleq P \times Q \times D$, rapidly increases with the SPSS aperture, Ξ, and the number of descriptors of the UC, D.

III. SPSS SYNTHESIS PROCEDURE

According to the mathematical formulation in Section II and referring to (1), the SPSS design is split into two steps [11], as usually done also in reflectarray engineering [15], [28], concerned with a macroscale constrained IS problem followed by a local current matching step. More specifically, the SPSS layout is synthesized by first computing the optimal reference current, $\mathbf{J}_{opt}^{tot}$, which radiates a far-field pattern, $\mathbf{F}_{opt}(\mathbf{r}) \triangleq \mathcal{L}\{\mathbf{J}_{opt}^{tot}(\mathbf{r})\}$, minimizing $\mathcal{O}[\mathbf{F}_{opt}(\mathbf{r})]$, and then finding the optimal setup of the SPSS descriptors, $\mathbf{G}_{opt}$, such that

$$\mathbf{G}_{opt} = \arg\left[\min_{\mathbf{G}}\{\Delta(\mathbf{G})\} \right] \quad (8)$$

where $\Delta(\mathbf{G})$ is the surface current mismatch ($\Delta(\mathbf{G}) \triangleq \|\mathbf{J}^{tot}(\mathbf{r}; \mathbf{G}) - \mathbf{J}_{opt}^{tot}(\mathbf{r})\|_{\Xi}^2$, $\|\cdot\|_{\Xi}$ being the ℓ_2-norm over Ξ given by $\|.\|_{\Xi} \triangleq \sqrt{\int_{\Xi} |.|^2 d\mathbf{r}}$).

The first step is carried out as in [11] by choosing an IPT-based approach [20] to find the optimal SPSS currents. Toward this end, the "pattern" feasibility space $\mathcal{W}\{\mathbf{F}(\mathbf{r})\}$ and the "current" feasibility space $\mathcal{W}\{\mathbf{J}^{tot}(\mathbf{r})\}$, as well as the mutual projection operators, are defined. The former, $\mathcal{W}\{\mathbf{F}(\mathbf{r})\}$, is cast into the following mask-matching form:

$$\mathcal{W}\{\mathbf{F}(\mathbf{r})\} \triangleq \left\{ \mathbf{F}(\mathbf{r}) : |\mathbf{F}(\mathbf{r})|^2 \geq \mathcal{M}(\mathbf{r}); \, \mathbf{r} \in \Theta \right\} \quad (9)$$

where $\mathcal{M}(\mathbf{r})$ is the user-defined lower footprint power mask in the coverage region Θ. Moreover, let us describe the feasibility space of the "current" as $\mathcal{W}\{\mathbf{J}^{tot}(\mathbf{r})\} \triangleq \{\mathbf{J}^{tot}(\mathbf{r}): \mathbf{J}^{tot}(\mathbf{r}) = C \exp[j\chi(\mathbf{r})]; \, \mathbf{r} \in \Xi\}$, C and $\chi(\mathbf{r})$ being the magnitude constant and the locally controlled phase distribution of the surface current, respectively.

The IPT synthesis process iteratively updates the ith ($i = 1, \ldots, I$) guess current, $\mathbf{J}_i^{tot}$ (i being the iteration index), starting from a random distribution, $\mathbf{J}_0^{tot}$, and alternatively computing the ith ($i = 1, \ldots, I$) "projected pattern," $\widetilde{\mathbf{F}}_i$ ($\mathbf{F}_i(\mathbf{r}) \triangleq \mathcal{L}[\mathbf{J}_i^{tot}(\mathbf{r})]$)

$$\widetilde{\mathbf{F}}_i(\mathbf{r}) = \begin{cases} \sqrt{\mathcal{M}(\mathbf{r})} & \text{if } |\mathbf{F}_i(\mathbf{r})|^2 \leq \mathcal{M}(\mathbf{r}) \\ \mathbf{F}_i(\mathbf{r}) & \text{otherwise} \end{cases} \quad (10)$$

and the "projected current" at the next $(i + 1)$th iteration

$$\mathbf{J}_{i+1}^{tot}(\mathbf{r}) = \frac{\mathbf{J}_i^{MN}(\mathbf{r})}{\left\|\mathbf{J}_i^{MN}(\mathbf{r})\right\|} \qquad (11)$$

where $\mathbf{J}_i^{MN}$ is the minimum norm solution of the integral equation (1) (i.e., $\mathbf{J}_i^{MN}(\mathbf{r}) \triangleq \mathcal{L}_{MN}^{-1}\{\widetilde{\mathbf{F}}_i(\mathbf{r})\}$), which is determined with the truncated singular value decomposition [25].

The process is stopped when either the maximum number of IPT iterations has been reached (i.e., $i = I$), or the value of the pattern matching index, Γ_i $(i < I)$, given by

$$\Gamma_i = \frac{\left\|\widetilde{\mathbf{F}}_i(\mathbf{r}) - \mathbf{F}_i(\mathbf{r})\right\|_{\Theta}}{\left\|\mathbf{F}_i(\mathbf{r})\right\|_{\Theta}} \qquad (12)$$

is smaller than a user-defined convergence threshold, γ, and the estimate of the surface current distribution is outputted by setting $\mathbf{J}_{opt}^{tot}(\mathbf{r}) = \mathbf{J}_i^{tot}(\mathbf{r})$, $\mathbf{r} \in \Xi$.

As for the second step toward the SPSS synthesis, solving (8) to find $\mathbf{G}_{opt}$ is a computationally challenging optimization task due to the number and the heterogeneity of the DoFs and the cost function at hand, $\Delta(\mathbf{G})$.[1] According to the guidelines in the global optimization literature (see, for instance, [4], [29] and the reference therein), an iterative SbD-based strategy is applied by generating a succession of N trial sets, $\{\mathcal{P}^{(n)}; n = 1, \dots, N\}$ (n being the iteration index during the optimization), with the Particle Swarm mechanism [29] and computing the current mismatch, $\Delta(\mathbf{G}^a|^{(n)})$, for each ath $(a = 1, \dots, A)$ guess SPSS layout of each nth $(n = 1, \dots, N)$ iteration/swarm being $\mathcal{P}^{(n)} = \{\mathbf{G}^a|^{(n)}; a = 1, \dots, A\}$, while A is the swarm size. The calculation of $\Delta(\mathbf{G}^a|^{(n)})$ requires the knowledge of the surface current $\mathbf{J}^{tot}$ in correspondence with the ath $(a = 1, \dots, A)$ layout of the nth $(n = 1, \dots, N)$ swarm, $\mathbf{G}^a|^{(n)}$ [i.e., $\mathbf{J}^{tot}(\mathbf{G}^a|^{(n)})$], which is accomplished once the electric and magnetic polarization surface densities, $\mathbf{S}^{e/m}(\mathbf{r}; \mathbf{G}^a|^{(n)})$, are determined through (3) and (4). Toward this end, the key task is to deduce the local surface susceptibility tensors of the (p, q)th $(p = 1, \dots, P; q = 1, \dots, Q)$ UC, $\overline{\overline{\psi}}_{pq}^{e/m}$, but depending on the whole SPSS arrangement [i.e., $\overline{\overline{\psi}}_{pq}^{e/m} = \overline{\overline{\psi}}_{pq}^{e/m}(\mathbf{G}^a|^{(n)})$]. Because of the computational costs, the use of a full-wave simulator is impossible since it would imply the expensive EM modeling of the behavior of $P \times Q \times A \times N$ full-size SPSSs. To reduce the computational burden, the EM response of the SPSS has been emulated with a UC-DT, which has been trained by exploiting a single-cell full-wave model under the assumption of periodic boundary conditions [11]. However, neglecting the aperiodicity and the edge effects of the actual finite-size SPSS introduces a nonnegligible degree of approximation. In order to avoid such a drawback and unlike [11], a Local UC-DT is defined to substitute the actual $\overline{\overline{\psi}}_{pq}^{e/m}(\mathbf{G})$ with its surrogate $\overline{\overline{\zeta}}_{pq}^{e/m}(\mathbf{G})$ learned offline from a small-scale model of the

SPSS. More specifically, such a Local UC-DT is implemented according to the following procedure.

- *Small-Scale SPSS Modeling:* An aperiodic $P' \times Q'$ (with $P' \ll P$, $Q' \ll Q$) small-scale SPSS layout, which is described by the reduced vector of descriptors $\mathbf{G}'$ ($\mathbf{G}' \triangleq \{\mathbf{g}_{p'q'}; p' = 1, \dots, P'; q' = 1, \dots, Q'\}$) whose (p', q')th entry is still of size D (i.e., $\mathbf{g}_{p'q'} \triangleq \{g_{p'q'}^{(d)}; d = 1, \dots, D\}$, is built.

- *Small-Scale SPSS Training Set Definition:* A representative set of B variations of the $P' \times Q'$ D-size small-scale descriptors is considered to derive B small-scale SPSS layouts $\{\mathbf{G}_b'; b = 1, \dots, B\}$; then, the behavior of each bth $(b = 1, \dots, B)$ layout is full-wave simulated to predict its EM behavior by extracting the corresponding susceptibility tensors $\{\overline{\overline{\psi}}_{p'q'}^{e/m}(\mathbf{G}_b'); p' = 1, \dots, P'; q' = 1, \dots, Q'\}$ (which are not affected by the direction of the incident wave) from the local scattering parameters [12].

- *Small-Scale SPSS AI-Based Surrogate Model Creation:* The AI-based Local UC-DT surrogate model $\overline{\overline{\zeta}}_{p'q'}^{e/m}(\mathbf{G}')$ $(p' = 1, \dots, P'; q' = 1, \dots, Q')$ is created starting from the small-scale B-size SPSS training set, $\{[\mathbf{G}_b', \overline{\overline{\psi}}_{p'q'}^{e/m}(\mathbf{G_b'})]; b = 1, \dots, B\}$, by means of a statistical learning approach based on the Ordinary Kriging (OK) method [15], [23]. More in detail, the value of $\overline{\overline{\zeta}}_{p'q'}^{e/m}(\mathbf{G}')$ $(p' = 1, \dots, P'; q' = 1, \dots, Q')$ is predicted as follows:

$$\begin{aligned}
\overline{\overline{\zeta}}_{p'q'}^{e/m}(\mathbf{G}') &= \wp_3^{reg}\left\{\psi_{p'q'}^{e/m}(\mathbf{G}_b'); \mathbf{c}\right\}\mathfrak{I}_{3\times3}^{unit} \\
&+ \left[\wp_B^{corr}\{\mathbf{G}'; \mathbf{c}\}\right]^{\dagger}\left[\mathfrak{I}_{B\times B}^{corr}\{\mathbf{G}_b'; \mathbf{c}\}\right]^{-1} \\
&\times \left(\mathfrak{I}_{B\times3}^{train}\left\{\psi_{p'q'}^{e/m}(\mathbf{G}_b')\right\} - \wp_B^{unit}\wp_3^{(4)}\times \right. \\
&\left. \times \left\{\psi_{p'q'}^{e/m}(\mathbf{G}_b'); \mathbf{c}\right\}\left\{\psi_{p'q'}^{e/m}(\mathbf{G}_b'); \mathbf{c}\right\}\right)\mathfrak{I}_{3\times3}^{unit}
\end{aligned}$$

(13)

where

$$\begin{aligned}
&\wp_3^{reg}\left\{\psi_{p'q'}^{e/m}(\mathbf{G}_b'); \mathbf{c}\right\} \\
&\triangleq \left(\left[\wp_B^{unit}\right]^{\dagger} \times \left[\mathfrak{I}_{B\times B}^{corr}\{\mathbf{G}_b'; \mathbf{c}\}\right]^{-1}\wp_B^{unit}\right)^{-1}\left[\wp_B^{unit}\right]^{\dagger} \\
&\times \left[\mathfrak{I}_{B\times B}^{corr}\{\mathbf{G}_b'; \mathbf{c}\}\right]^{-1}\mathfrak{I}_{B\times3}^{train}\left\{\psi_{p'q'}^{e/m}(\mathbf{G}_b')\right\}
\end{aligned} \qquad (14)$$

is the regression parameter matrix,[2] $\wp_B^{corr}\{\mathbf{G}'; \mathbf{c}\}$ is the B-size exponential correlation vector ($\wp_B^{corr}\{\mathbf{G}'; \mathbf{c}\} \triangleq \{Z_b(\mathbf{G}'; \mathbf{c}) = \exp(-\sum_{p'=1}^{P'}\sum_{q'=1}^{Q'}\sum_{d=1}^{D} c_n |g_{p'q'}^{(d)} - g_{p'q'}^{(d)}|_b|); b = 1, \dots, B\}$ being $n = p'+P'\times(q'-1)+P'\times Q'\times(d-1)$), and $\mathfrak{I}_{B\times B}^{corr}\{\mathbf{G}_b'; \mathbf{c}\}$ is a $B \times B$ matrix whose bth $(b = 1, \dots, B)$ column is equal to $\wp_B^{corr}\{\mathbf{G}'; \mathbf{c}\}$, while $\mathbf{c} \triangleq \{c_n; n = 1, \dots, \mathcal{N}\}$ is the set of $\mathcal{N}$ control parameters ($\mathcal{N}$ being the number of unknowns of the OK model, which corresponds to the number of design DoFs $P \times Q \times D$), which are automatically optimized during the OK self-tuning [23]. Moreover, $\mathfrak{I}_{B\times3}^{train}\{\psi_{p'q'}^{e/m}(\mathbf{G}_b')\}$ is the training-set matrix whose (w, b)th $(w = x, y, z; b = 1, \dots, B)$ entry is equal to the (ww)th component

---

[1]It is worthwhile to point out that the second step of the design process is formulated as the solution to a current matching problem with respect to the microscale UC geometry [i.e., (8)], rather than an ideal surface impedance matching one. Consequently, no physical constraint on the feasible surface reactance must be enforced in the procedure since no target surface reactance is actually computed.

[2]For notation simplicity, the symbol $\mathfrak{I}_{u\times v}$ is used to indicate a matrix of u rows and v columns, while $\wp_u$ identifies a vector of u rows.
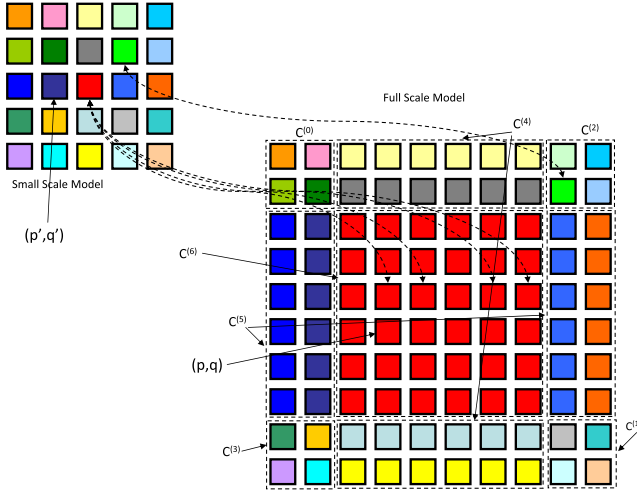
Fig. 2. Illustrative example—example of local UC-DT mapping between the small-scale model ($P' \times Q' = 5 \times 5$) and the full-scale SPSS arrangement ($P \times Q = 10 \times 10$).

of the local surface susceptibility diagonal tensor of the (p', q')th UC of the bth small-scale SPSS layout, $\mathbf{G}'_b$, (i.e., $\Im^{train}_{B \times 3} \{ \psi^{e/m}_{p'q'}(\mathbf{G}'_b) \} \triangleq \{ \psi^{e/m}_{p'q'}(\mathbf{G}'_b) |_{ww}; \; w = x, y, z; \; b = 1, \ldots, B \}$) being [11], [12]

$$\overline{\overline{\psi}}^{e/m}_{p'q'}(\mathbf{G}'_b) \triangleq \sum_{w=x,y,z} \psi^{e/m}_{p'q'}(\mathbf{G}'_b) \Big|_{ww} \widehat{w}\widehat{w} \qquad (15)$$

while $\wp^{unit}_B$ is a unitary column vector of length B and $\cdot^\dagger$ stands for the transpose operator.

- *Small-Scale to Full-Scale SPSS Prediction Mapping:* The actual local surface susceptibility tensors of the full-size SPSS, $\{ \overline{\overline{\psi}}^{e/m}_{pq}(\mathbf{G}); \; p = 1, \ldots, P; \; q = 1, \ldots, Q \}$, are then estimated by deriving $\{ \overline{\overline{\zeta}}^{e/m}_{pq}(\mathbf{G}); \; p = 1, \ldots, P; \; q = 1, \ldots, Q \}$ from the OK small-scale SPSS predictions, $\{ \overline{\overline{\zeta}}^{e/m}_{p'q'}(\mathbf{G}'); \; p' = 1, \ldots, P'; \; q' = 1, \ldots, Q' \}$ according to the mapping scheme pictorially illustrated in Fig. 2 and performed according to the rules in the Appendix.

Once the Local UC-DT has been implemented offline and it is available, the SbD-based SPSS synthesis process can be efficiently executed, even multiple times, without recurring to additional full-wave simulations of either a part or the whole of the UCs arrangement. Moreover, no further training is required even if the synthesis objectives $\mathcal{O}[\mathbf{F}(\mathbf{r}; \mathbf{G})]$ are changed after the Local UC-DT was created. Those features assure the arising design method high-scalability and reusability properties.

IV. NUMERICAL RESULTS

In this section, a selected set of examples from a wide numerical analysis is reported to illustrate the proposed AI-enhanced aperiodic microscale design procedure for the synthesis of SPSSs working in real scenarios and to assess the reliability of the synthesized layouts in operative conditions through full-wave simulations. More specifically, the numerical validation has been carried out by considering various supports of the SPSS and different radiation objectives, $\mathcal{O}[\mathbf{F}(\mathbf{r}; \mathbf{G})]$. As for this latter, the pencil coverage and shaped coverage cases have been chosen since as

largely representative of several real applications.[3] In the pencil coverage case, the power reflected by the SPSS is focused toward the desired (anomalous non-Snell) target direction, (θ^T, φ^T), which means setting $\mathcal{O}[\mathbf{F}(\mathbf{r}; \mathbf{G})] = \mathcal{O}^{pen}[\mathbf{F}(\mathbf{r}; \mathbf{G})]$ $(\mathcal{O}^{pen}[\mathbf{F}(\mathbf{r}; \mathbf{G})] \triangleq (1/|\mathbf{F}(r^T, \theta^T, \varphi^T; \mathbf{G})|^2)$, where r^T is an arbitrary (far-field) distance, while $| \cdot |$ stands for the vector magnitude) and $\Theta = (r^T, \theta^T, \varphi^T)$ in (9). Otherwise, the SPSS of the shaped coverage case maximizes the reflected power in the user-defined footprint/coverage area Θ (see Fig. 1); thus, the synthesis objective is set to $\mathcal{O}[\mathbf{F}(\mathbf{r}; \mathbf{G})] = \mathcal{O}^{sha}[\mathbf{F}(\mathbf{r}; \mathbf{G})]$ $(\mathcal{O}^{sha}[\mathbf{F}(\mathbf{r}; \mathbf{G})] \triangleq (1/\int_\Omega |\mathbf{F}(\mathbf{r}); \mathbf{G}|^2 d\mathbf{r}))$. Finally, $\mathcal{M}(\mathbf{r}) = 0$ [dB] has been set in both cases.

Concerning the benchmark SEE scenario, a base station has been assumed to illuminate the SPSS at $f = 3.5$ [GHz] (i.e., sub-6 GHz $n78$ band [30]) with a plane wave featuring circular polarization (i.e., $E^{inc}_{TE} = 1$ and $E^{inc}_{TM} = j$) and impinging from broadside (i.e., $(\theta^{inc}, \varphi^{inc}) = (0, 0)$ [deg] $\rightarrow \widehat{\mathbf{e}}_{TE} = \widehat{\mathbf{y}}$ and $\widehat{\mathbf{e}}_{TM} = \widehat{\mathbf{x}}$). Moreover, the calibration parameters of the synthesis procedure have been set following the guidelines in [11], [15]: $B = 2 \times 10^4$,[4] $\gamma = 10^{-4}$, $I = 10^3$, $A = 10$, and $N = 10^4$. Finally, the full-wave simulations have been carried out with Ansys HFSS [24].

In order to illustrate the proposed SPSS design method, let start with the off-line process of building the local UC-DT, which does not depend on the synthesis objective (i.e., $\mathcal{O}[\mathbf{F}(\mathbf{r}; \mathbf{G})]$), to be defined for the (second) step of the SbD-based SPSS layout synthesis and kept in all numerical tests. Accordingly, a UC consisting of a metallic square patch of side ℓ ($D = 1$) printed on a Rogers RT/duroid 5870 laminate with thickness $\tau = 3.175 \times 10^{-3}$ [m] [see Fig. 3(a)] has been selected as the benchmark SPSS element. It can be noticed [see Fig. 3(c)–(d)] that the phase coverage of such a UC, which presents a structural resonance centered around $\ell = 2.5 \times 10^{-2}$ [m], is not complete [i.e., ≈ 330 [deg] at $f = 3.5$ GHz—Fig. 3(c)] as a consequence of the simple shape and the single-layer design. The choice of a basic/elementary UC has been made to assess the effectiveness of the proposed approach without the bias of a high-performance UC. Then, a small-scale SPSS layout with $P' \times Q' = 5 \times 5$ UCs $[g^{(d)}_{p'q'}]_{d=1} = \ell_{p'q'}$—Fig. 3(b)], arranged on a uniform lattice with periodicity $\Delta x = \Delta y = 4.28 \times 10^{-2}$ [m], has been defined ("small-scale SPSS modeling") and simulated in a full-wave fashion taking into account the copper thickness ($\nu = 35 \times 10^{-6}$ [m]) as well. Toward this end, the size of the small-scale model $P' \times Q'$ has been chosen following the procedure in [31] to guarantee an adequate tradeoff between performance stability and computational complexity. The B-sized OK training dataset has been built by varying the $P' \times Q'$ patch sides [i.e., $\ell_{p'q'}$ ($p' = 1, \ldots, P'$; $q' = 1, \ldots, Q'$)] of the small-scale SPSS layout ("small-scale SPSS training set definition"). Starting from this training set, an OK-based surrogate of the small-scale SPSS model has been built

---

[3]It is worth remarking that the solution process is independent on $\mathcal{O}[\mathbf{F}(\mathbf{r}; \mathbf{G})]$.

[4]As regards the number of samples in the training process, the value has been chosen according to the analysis carried out in [11] and [15] to guarantee a suitable tradeoff between time saving, model size, and prediction accuracy.
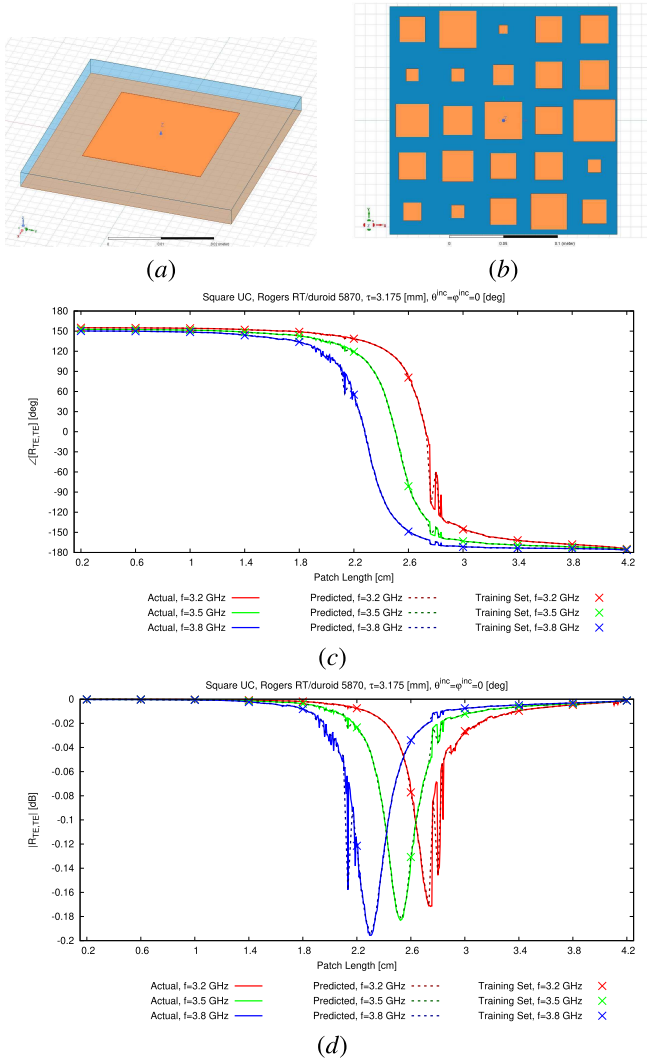
(a)

(b)

(c)

(d)

Fig. 3. Illustrative example—model of (a) UC of the SPSS and (b) small-scale SPSS layout. (c) Phase, $\angle \widetilde{R}_{TE,TE}$, and (d) magnitude, $\| \widetilde{R}_{TE,TE} \|$, of the average "TE-TE" reflection coefficient of the central element $[(p', q') = (P' + 1/2, Q' + 1/2)]$ of the small-scale SPSS layout.

by deriving $\overline{\overline{\zeta}}_{p'q'}^{e/m}(\mathbf{G}')$ ($p' = 1, \ldots, P'$; $q' = 1, \ldots, Q'$). Some insights on the accuracy of the arising predictor can be inferred by the plots of the phase [see Fig. 3(c)] and the magnitude [see Fig. 3(d)] of the average "TE–TE" reflection coefficient of a representative element [i.e., the central one located at $(p', q') = ((P' + 1/2), (Q' + 1/2))$] of the small-scale SPSS layout

$$\widetilde{R}_{p'q'}^{TE,TE} = \frac{1}{B} \sum_{b=1}^{B} R^{TE,TE} \left[\overline{\overline{\psi}}_{p'q'}^{e/m}(\mathbf{G}'_b)\right]_{p'=\frac{P'+1}{2}}^{q'=\frac{Q'+1}{2}}. \quad (16)$$

As it can be observed, the predicted curve (i.e., $\widetilde{R}_{p'q'}^{TE,TE} = (1/B) \sum_{b=1}^{B} R^{TE,TE} [\overline{\overline{\zeta}}_{p'q'}^{e/m}(\mathbf{G}'_b)]_{p'=(P'+1/2)}^{q'=(Q'+1/2)}$) faithfully matches the actual one passing throughout the "training" samples as expected from the OK theory and carefully replicating the overall phase trend including the minor phase discontinuities caused by the unavoidable numerical approximations in the HFSS simulations. The obtained accuracy, which quantitatively corresponds to a $\leq 0.1\%$ error on the prediction of the phase of the average "TE-TE" reflection coefficient [see Fig. 3(c)], is actually expected due to the relatively simple
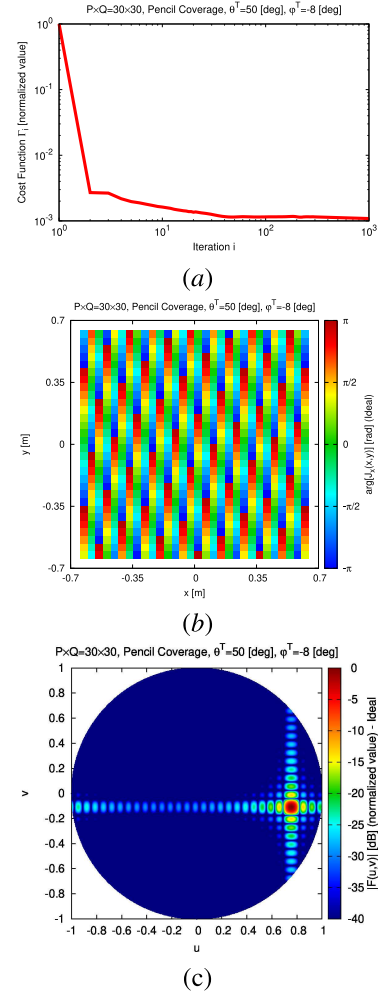

(a)

(b)

(c)

Fig. 4. Illustrative example (pencil coverage, $P = Q = 30$, $\theta^T = 50$ [deg], $\varphi^T = -8$ [deg], $H = 5$ [m])—(a) evolution of the pattern matching index, Γ_i ($i = 1, \ldots, I$) and of (b) reference surface current distribution (x-component), and $J_x^{opt}(\mathbf{r}) \triangleq \mathbf{J}_{opt}^{tot}(\mathbf{r}) \cdot \hat{\mathbf{x}}$ ($\mathbf{r} \in \Xi$), with (c) radiated far-field pattern in the (u, v) plane, $|\mathbf{F}_{opt}(\mathbf{r})|$ (1).

geometrical feature of the cell [see Fig. 3(a)], as anticipated in the state-of-the-art on UC-DTs [23]. The interested reader is referred to [23] for additional guidelines regarding the expected OK accuracy when dealing with more complex UCs.

Once the "small-scale SPSS AI-based surrogate model" has been created, it is then possible to deal with the SEE problem at hand, which is user-defined by setting the macroscale radiation objectives (i.e., $\mathcal{O}[\mathbf{F}(\mathbf{r}; \mathbf{G})]$) and the SPSS support and position in the global reference system of coordinates (x_{glob}, y_{glob}, z_{glob}) (see Fig. 1).

The first test case of the numerical assessment is concerned with the synthesis of an SPSS installed at $H = 5$ [m] over the ground (see Fig. 1) with $P \times Q = 30 \times 30$ UCs (i.e., $\Xi \approx 1.28 \times 1.28$ [m²]) to yield a pencil coverage with focusing direction $(\theta^T, \varphi^T) = (50, -8)$ [deg], which corresponds to a footprint spot at $x_{glob} = -35.7$ [m], $y_{glob} = 30.14$ [m]. By following the procedure described in Section III, the first step has been carried out with the IPT [see Fig. 4(a)] to compute the optimal reference current, $\mathbf{J}_{opt}^{tot}$ [see Fig. 4(b)[5]],

[5]For symmetry reasons, the two components of the surface current are identical. Thus, only the x-component, $J_x^{tot}(\mathbf{r})$, will be shown.

(a)

(c)
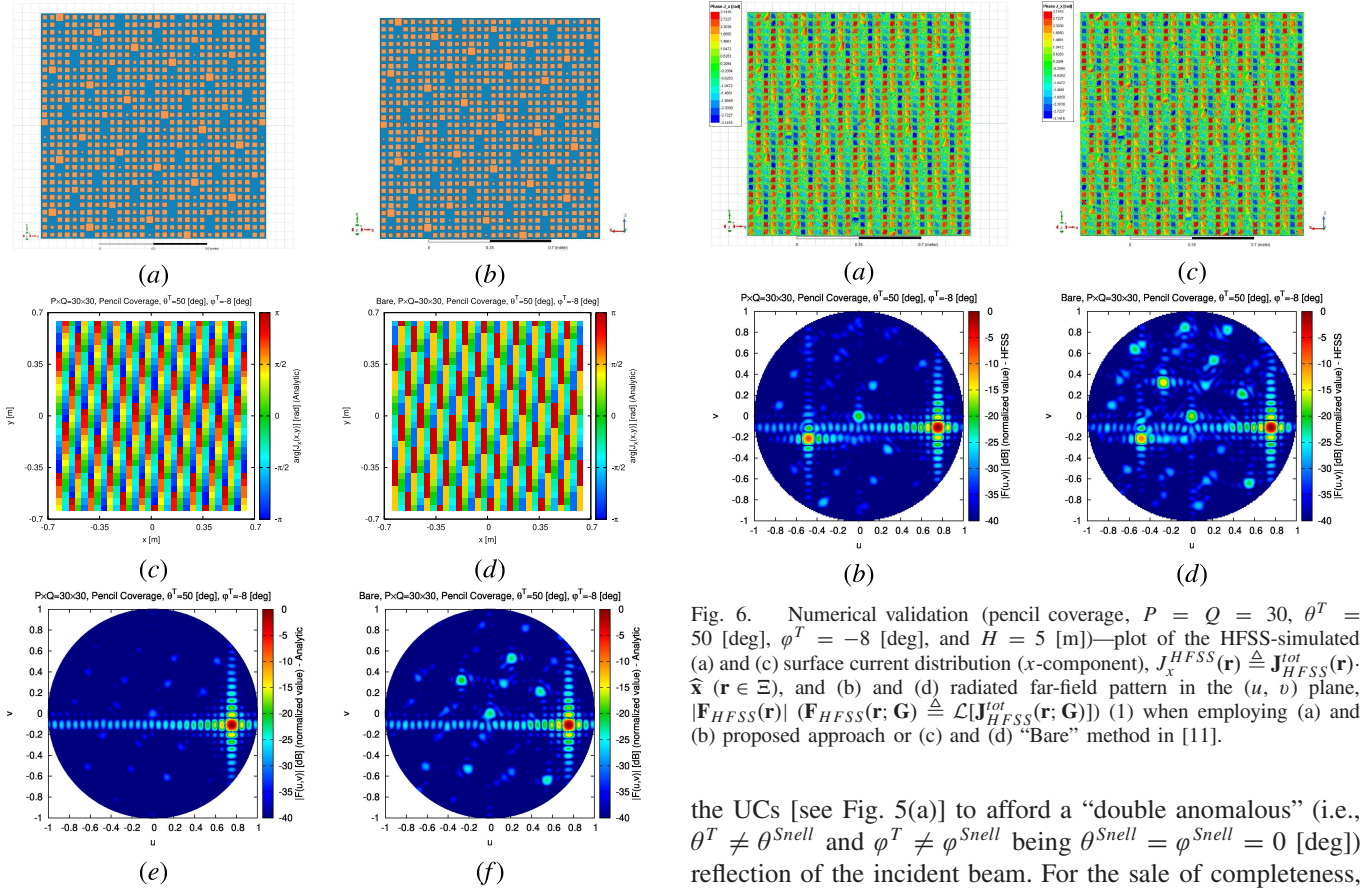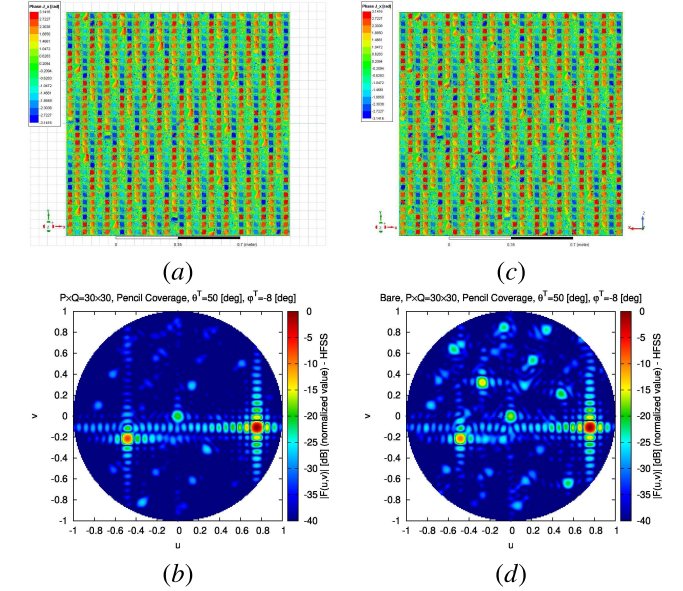

(b)

(d)

Fig. 6. Numerical validation (pencil coverage, $P = Q = 30$, $\theta^T = 50$ [deg], $\varphi^T = -8$ [deg], and $H = 5$ [m])—plot of the HFSS-simulated (a) and (c) surface current distribution (x-component), $J_x^{HFSS}(\mathbf{r}) \triangleq \mathbf{J}_{HFSS}^{tot}(\mathbf{r}) \cdot \hat{\mathbf{x}}$ ($\mathbf{r} \in \Xi$), and (b) and (d) radiated far-field pattern in the (u, v) plane, $|\mathbf{F}_{HFSS}(\mathbf{r})|$ ($\mathbf{F}_{HFSS}(\mathbf{r}; \mathbf{G}) \triangleq \mathcal{L}[\mathbf{J}_{HFSS}^{tot}(\mathbf{r}; \mathbf{G})]$) (1) when employing (a) and (b) proposed approach or (c) and (d) "Bare" method in [11].

(a)

(b)

(c)

(d)

(e)

(f)

Fig. 5. Illustrative example (pencil coverage, $P = Q = 30$, $\theta^T = 50$ [deg], $\varphi^T = -8$ [deg], and $H = 5$ [m])—(a) and (b) synthesized SPSS layout and the corresponding (c) and (d) surface current distribution (x-component), $J_x^N(\mathbf{r}) \triangleq \mathbf{J}_N^{tot}(\mathbf{r}) \cdot \hat{\mathbf{x}}$ ($\mathbf{r} \in \Xi$), and (e) and (f) radiated far-field pattern in the (u, v) plane, $|\mathbf{F}_N(\mathbf{r})|$ ($\mathbf{F}_N(\mathbf{r}; \mathbf{G}) \triangleq \mathcal{L}[\mathbf{J}_N^{tot}(\mathbf{r}; \mathbf{G})]$) (1), when employing (a), (c), and (e) proposed approach or (b), (d), and (f) "Bare" method in [11].

which radiates the far-field pattern $\mathbf{F}_{opt}(\mathbf{r}) \triangleq \mathcal{L}\{\mathbf{J}_{opt}^{tot}(\mathbf{r})\}$ [see Fig. 4(c)] by minimizing $\mathcal{O}^{pen}[\mathbf{F}_{opt}(\mathbf{r})]$.

Fig. 4(a) shows that there is a quick reduction of the value of the pattern matching index Γ_i (12) ($i = 1, \ldots, I$), which confirms the effectiveness of the IPT when applied to fulfill macroscale objectives (i.e., reflection performance) by optimizing microscale DoFs (i.e., the surface currents). It is also worth pointing out that the synthesized current distribution only depends on the project targets and not on the UC geometry; hence, the same surface current can be kept also varying the UC materials, shapes, layers, and so on. In the second step of the SPSS synthesis, the layout in Fig. 5(a) has been derived from the SbD-driven optimization of the UC descriptors to match the reference current profile in Fig. 4(b). As a matter of fact, the arising surface current, $\mathbf{J}_N^{tot}$ [see Fig. 5(c)], turns out to be very close to the reference one, the same similarity being present between the radiated far-field patterns in the (u, v)-domain ($u \triangleq \sin\theta\cos\varphi$ and $v \triangleq \sin\theta\sin\varphi$) [see Figs. 5(e) versus 4(c)]. Both outcomes confirm the effectiveness of the optimization process that allows the designer to analytically synthesize a large SPSS (i.e., 30×30 UCs) with a careful control of the resulting reflection/focusing properties. As for this latter item, it turns out that there is the need of a nonuniform arrangement of

the UCs [see Fig. 5(a)] to afford a "double anomalous" (i.e., $\theta^T \neq \theta^{Snell}$ and $\varphi^T \neq \varphi^{Snell}$ being $\theta^{Snell} = \varphi^{Snell} = 0$ [deg]) reflection of the incident beam. For the sake of completeness, the layout [see Fig. 5(b)], surface currents [see Fig. 5(d)], and resulting far-field pattern in the (u, v)-domain [see Fig. 5(e)] obtained by the "bare" approach in [11] are reported in Fig. 5, as well. As it can be noticed and as expected from the theoretical viewpoint, the state-of-the-art technique yields a suboptimal effectiveness both in terms of $\mathbf{J}_N^{tot}$ [see Figs. 5(d) versus 4(b)] and $|\mathbf{F}_N(\mathbf{r})|$ [see Figs. 5(f) versus 4(c)] with respect to the proposed technique [e.g., Fig. 5(f) versus (e)].

In order to assess the reliability of the synthesis process and the effectiveness of the arising design, the SPSS layout has been also HFSS-modeled, and the results have been compared in terms of surface currents (i.e., the target of the second step) [see Figs. 6(a) versus 5(b)] and far-field reflected power patterns [see Figs. 6(b) versus 5(c)], as well as footprint patterns (i.e., the objective of the whole synthesis process) [see Fig. 7(b) versus (a)]. As expected, the plot of the full-wave simulated pattern [see Fig. 6(b)] confirms that the synthesized SPSS is able to focus the reflected beam along the desired anomalous direction [i.e., $(u^T, v^T) = (7.58 \times 10^{-1}, -1.06 \times 10^{-1})$ being $u^T = \sin\theta^T\cos\varphi^T$ and $v^T = \sin\theta^T\sin\varphi^T$]. Moreover, the HFSS plot indirectly proves the accuracy of the SPSS surrogate since the far-field distributions are very similar [see Figs. 6(b) versus 5(c)] within the whole visible domain except for a minor secondary lobe located at $u \in [-0.5, -0.4]$, $v \in [-0.3, -0.2]$ [see Fig. 6(b)] possibly caused by the higher order modes arising in the SPSS UC patches and not taken into account in Section II. Furthermore, the plots of the same quantities obtained by the smart skin designed by means of the state-of-the-art method in [11]
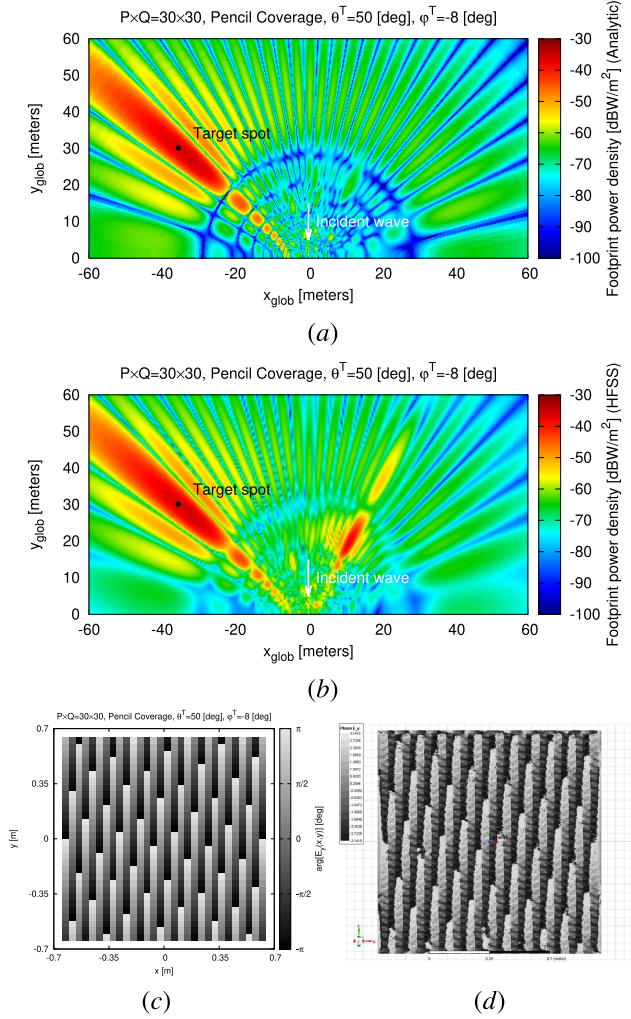
Fig. 7. Numerical validation (pencil coverage, $P = Q = 30$, $\theta^T = 50$ [deg], $\varphi^T = -8$ [deg], and $H = 5$ [m])—(a) and (b) SPSS footprint pattern and of (c) and (d) component of the surface averaged electric field (5), $\{\mathbf{E}_{pq}^{ave}(\mathbf{G}); p = 1, \ldots, P; q = 1, \ldots, Q\}$, and (a) and (c) analytically computed or (b) and (d) HFSS-simulated.
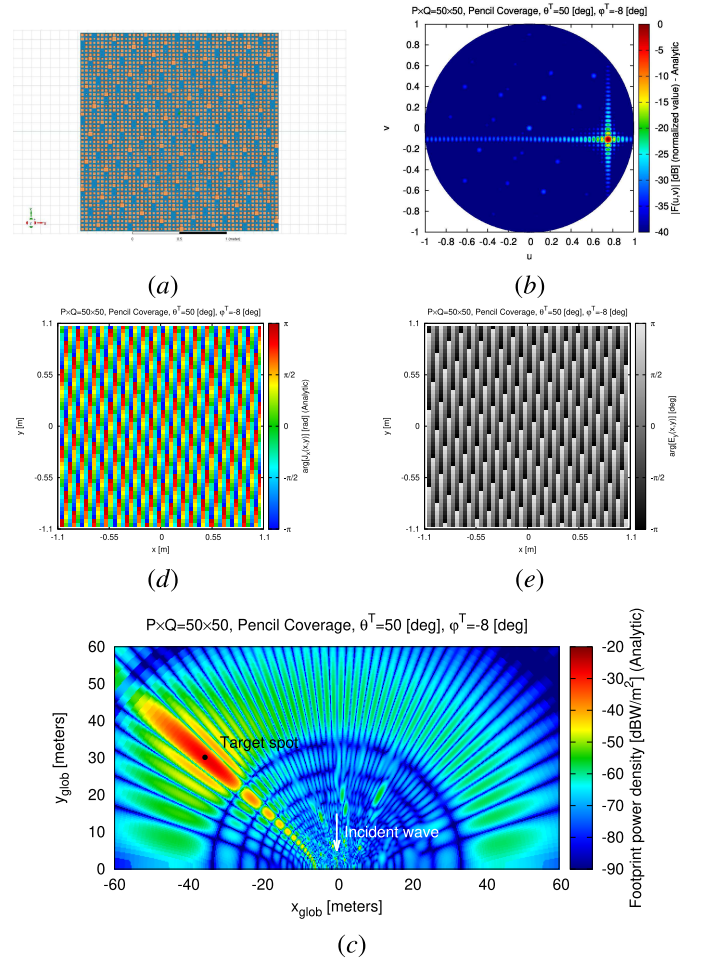
Fig. 8. Numerical validation (pencil coverage, $P = Q = 50$, $\theta^T = 50$ [deg], $\varphi^T = -8$ [deg], and $H = 5$ [m])—(a) synthesized SPSS layout and the corresponding (b) far-field pattern in the (u, v) plane, $|\mathbf{F}_N(\mathbf{r})|$ ($\mathbf{F}_N(\mathbf{r}; \mathbf{G}) \triangleq \mathcal{L}[\mathbf{J}_N^{tot}(\mathbf{r}; \mathbf{G})]$) (1), (c) SPSS footprint pattern, (d) surface current distribution (x-component), $J_x^N(\mathbf{r}) \triangleq \mathbf{J}_N^{tot}(\mathbf{r}) \cdot \hat{\mathbf{x}}$ ($\mathbf{r} \in \Xi$), and (e) y-component of the surface averaged electric field (5), $\{\mathbf{E}_{pq}^{ave}(\mathbf{G}); p = 1, \ldots, P; q = 1, \ldots, Q\}$.

further confirm the suboptimal performance of such a strategy with respect to the proposed synthesis approach [e.g., Fig. 6(d) versus (b)]. The reliability of the designed SPSS is further confirmed by the analytically computed [see Fig. 7(a)] and HFSS-simulated [see Fig. 7(b)] footprint power densities analyzed in an area of extension 120×60 [m^2] in front of the smart skin. Both indicate that the peak of the reflected power is maximum within the coverage spot centered at $x_{glob} = -35.7$ [m] and $y_{glob} = 30.14$ [m] with close values of the directivity index (i.e., $\xi^{pen} = 32.52$ [dB] [see Fig. 7(a)] versus $\xi_{HFSS}^{pen} = 31.91$ [dB] [see Fig. 7(b)], being $\xi^{pen} \triangleq (4\pi r^2 |\mathbf{F}(\mathbf{r}; \mathbf{G})|^2 / \int_0^{2\pi} \int_0^\pi |\mathbf{F}(\mathbf{r}; \mathbf{G})|^2 r^2 \sin(\theta) d\theta d\varphi$ the average directivity in the footprint region for the SEE pencil coverage). Moreover, despite the approximations of the analytic approach (see Section II) in modeling the surface currents on Ξ, there is a good agreement between the current distributions [see Figs. 6(a) versus 5(b)] and the surface averaged fields (5) $\{\mathbf{E}_{pq}^{ave}(\mathbf{G}); p = 1, \ldots, P; q = 1, \ldots, Q\}$ [see Fig. 7(c) versus (d)]. This further assesses the effectiveness of the "Small-Scale to Full-Scale SPSS Prediction Mapping"

step in predicting the actual local surface susceptibility tensors of the full-size SPSS, $\{\overline{\overline{\psi}}_{pq}^{e/m}(\mathbf{G}); p = 1, \ldots, P; q = 1, \ldots, Q\}$, both $\mathbf{J}^{tot}(\mathbf{r}; \mathbf{G})$ and $\mathbf{E}_{pq}^{ave}(\mathbf{G})$ being related to $\overline{\overline{\psi}}_{pq}^{e/m}(\mathbf{G})$ through (2)–(4) and (5), respectively.

The synthesis of a larger $P \times Q = 50 \times 50$ layout (i.e., $\Xi \approx 2.14 \times 2.14$ [m^2]) has been performed next to analyze the method robustness when dealing with higher dimensionalities of the optimization problem, $\mathcal{N}$ being proportional to $P \times Q$, as well as the dependence of the focalization features on the size of the SPSS support. Let us take a look to the SbD-synthesized layout in Fig. 8(a). Analogous to the $P = Q = 30$ case [see Fig. 5(a)], once again, the UCs are nonuniform, and the patterned surface appears (similarly) irregular as actually expected since the same anomalous coherent reflection of the previous test case is required-and-obtained here [see Fig. 8(b)] even though by exploiting a wider aperture. The larger SPSS support implies that the majority of the reflected power along the same desired direction ($u^T = 7.58 \times 10^{-1}$ and $v = -1.06 \times 10^{-1}$) is focused in a narrower beam [see Figs. 8(b) versus 5(c)] and a more confined coverage footprint [see Figs. 8(c) versus 7(a)]. Quantitatively, the
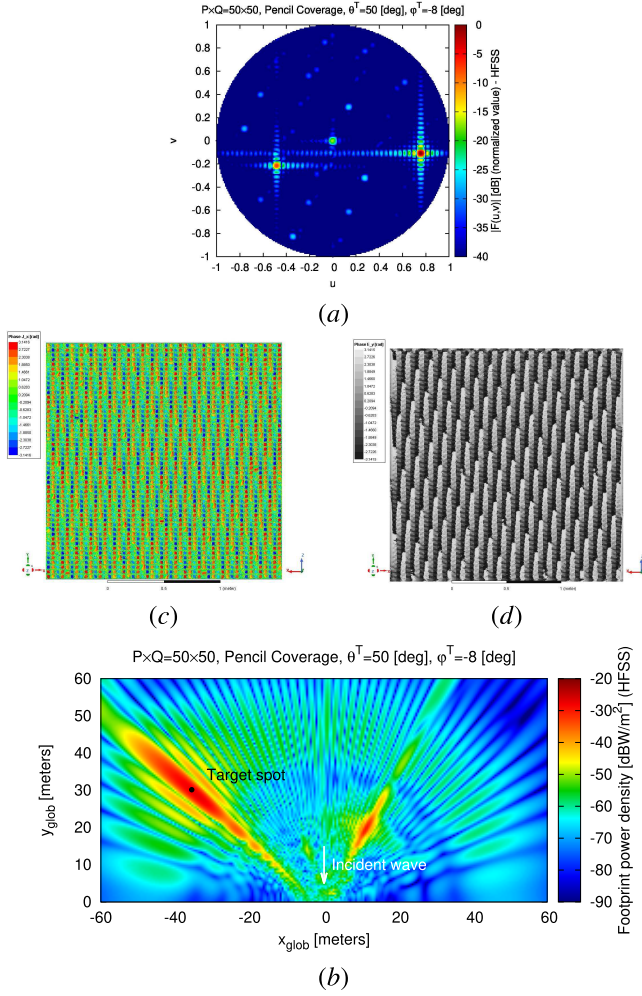
(a)

(c) (d)

(b)

Fig. 9. Numerical validation (pencil coverage, $P = Q = 50$, $\theta^T = 50$ [deg], $\varphi^T = -8$ [deg], and $H = 5$ [m])—plot of the HFSS-simulated (a) far-field pattern in the (u, v) plane, $|\mathbf{F}_{HFSS}(\mathbf{r})|$ ($\mathbf{F}_{HFSS}(\mathbf{r}; \mathbf{G}) \triangleq \mathcal{L}[\mathbf{J}_{HFSS}^{tot}(\mathbf{r}; \mathbf{G})]$) (1), (b) SPSS footprint pattern, (c) surface current distribution (x-component), $J_x^{HFSS}(\mathbf{r}) \triangleq \mathbf{J}_{HFSS}^{tot}(\mathbf{r}) \cdot \widehat{\mathbf{x}}$ ($\mathbf{r} \in \Xi$), and (e) y-component of the surface averaged electric field (5), $\{\mathbf{E}_{pq}^{ave}(\mathbf{G}); p = 1, \ldots, P; q = 1, \ldots, Q\}$.

increase in the SPSS area [$(\Xi_{P=Q=50}/\Xi_{P=Q=30}) \approx 2.77 \rightarrow \delta\Xi = 4.42$ [dB]—Figs. 8(a) versus 5(a)] corresponds to a proportional improvement of the focusing efficiency ($\delta\xi^{pen} \approx 4.5$ [dB]) being $\xi^{pen}\rfloor_{P=Q=50} = 36.96$ [dB] [see Fig. 8(c)] and $\xi^{pen}\rfloor_{P=Q=30} = 32.52$ [dB] [see Fig. 7(a)]). Such a result ($\delta\Xi \approx \delta\xi^{pen}$) can provide useful guidelines on how to size and design the SPSSs for obtaining the desired (selective/broad) coverage in an SEE scenario.

The same conclusions drawn in the first example on the reliability of the synthesis results hold true also for this wider SPSS as confirmed by the comparisons with the HFSS simulations, at microscale, of the spatial distributions of both the surface current, $\mathbf{J}^{tot}(\mathbf{r}; \mathbf{G})$ [see Figs. 9(c) versus 8(d)], and the averaged electric field, $\mathbf{E}_{pq}^{ave}(\mathbf{G})$ [see Figs. 9(d) versus 8(e)], while at macroscale, of the radiated patterns [see Figs. 9(a) versus 8(b)] and footprints [see Figs. 9(b) versus 8(c)]. For instance, it turns out that $\xi_{HFSS}^{pen} = 36.08$ [dB] $\approx \xi^{pen} = 36.96$ [dB] so that the rule $\delta\Xi \approx \delta\xi_{HFSS}^{pen}$ is verified also here.

But what about more complex footprints? The design of SPSSs for shaped coverages is, thus, discussed by considering
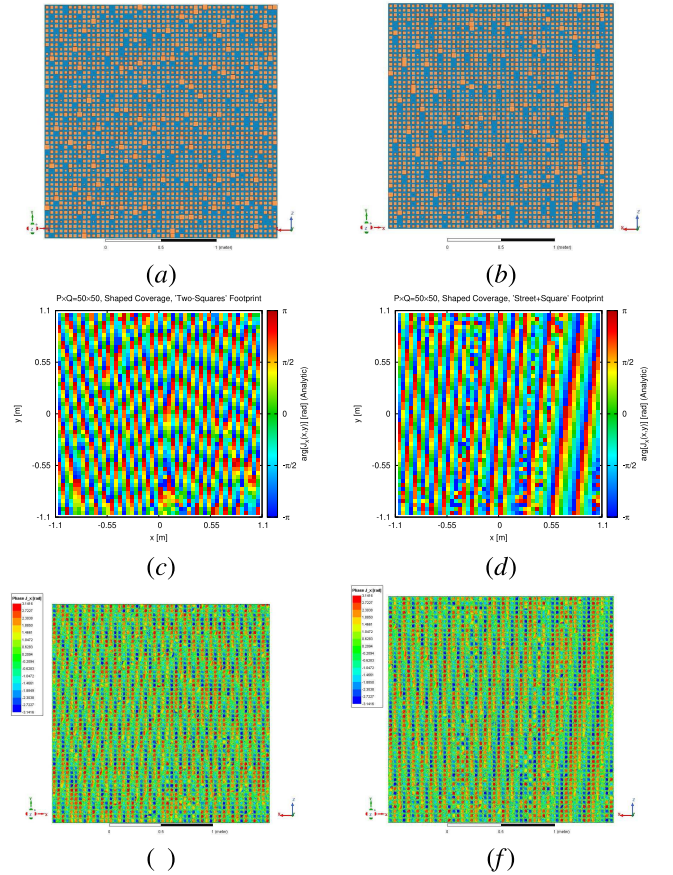

(a) (b)

(c) (d)

( ) (f)

Fig. 10. Numerical validation (shaped coverage, $P = Q = 50$ and $H = 5$ [m])—(a) and (b) synthesized SPSS layouts along with the corresponding (c) and (d) analytically computed or (e) and (f) HFSS-simulated surface current distributions (x-component), $J_x^{HFSS}(\mathbf{r}) \triangleq \mathbf{J}_{HFSS}^{tot}(\mathbf{r}) \cdot \widehat{\mathbf{x}}$ ($\mathbf{r} \in \Xi$) for (a), (c), and (e) the "two-square" and (b), (d), and (f) "street-square" footprints.

two different applicative scenarios, each with a different setup of the pattern-mask region Θ in (9) while keeping the same SPSS aperture ($P \times Q = 50 \times 50$). More specifically, the former ("Two-Squares Footprint" scenario) mimics the realistic case where the SPSS is requested to afford two separate and asymmetric beams that focus the power in very narrow, but shaped, regions, which emulates two small town squares in a urban environment. Numerically, Θ consists of two regions of 20×10 [m²] centered at $(x_{glob}^{(1)}, y_{glob}^{(1)}) = (-30, 15)$ [m] and $(x_{glob}^{(2)}, y_{glob}^{(2)}) = (28, 17)$ [m], respectively. Otherwise, the coverage region of the "Street-Square Footprint" case maps a 10×120 [m²] street centered at $(x_{glob}^{(1)}, y_{glob}^{(1)}) = (-35, 80)$ [m] that opens on a square of size 30×30 [m²] located at $x_{glob}^{(2)} = -y_{glob}^{(2)} = -45$ [m]. From a methodological viewpoint, such a test case is devoted to assess the potentialities of the SPSS in focusing the power in a region characterized by both complex contours and very low grazing angles, which are almost parallel to the ground surface, due to both the street position and length ($L_{street} = 140$ [m]) and the SPSS height above the ground ($H = 5$ [m]).

The layouts of the synthesized SPSSs [see Fig. 10(a)—"two-squares footprint"; Fig. 10(b)—"street-square footprint"] are still nonuniform but less regular than in the "pencil coverage" case [see Figs. 5(a) and 8(a)] due
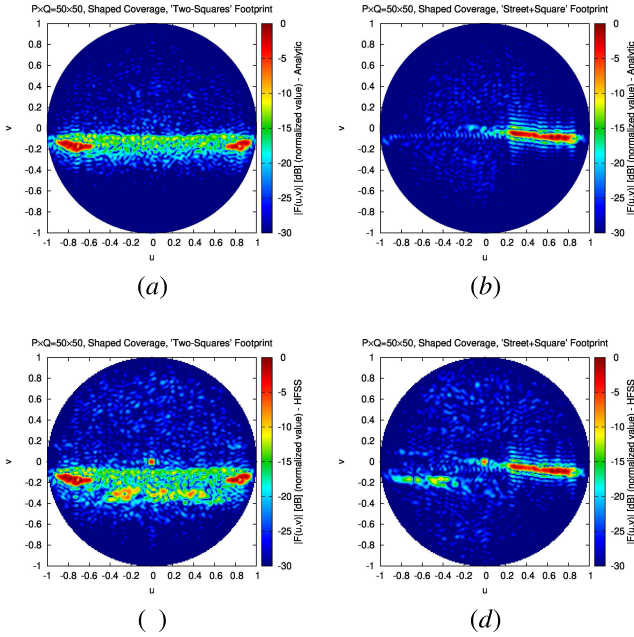
Fig. 11. Numerical validation (shaped coverage, $P = Q = 50$ and $H = 5$ [m])—(a) and (b) analytically computed and (c) and (d) HFSS-simulated far-field patterns in the (u, v) plane, $|\mathbf{F}(\mathbf{r})|$ ($\mathbf{F}(\mathbf{r}; \mathbf{G}) \triangleq \mathcal{L}[\mathbf{J}^{tot}(\mathbf{r}; \mathbf{G})]$) (1) for (a) and (c) "two-square" and (b) and (d) "street-square" footprints.

to the complexity of the shaped beam. As a consequence, the "periodicity" of the spatial behavior of the surface currents in Fig. 8(d) is completely lost [see Fig. 10(c)–(d)]. On the other hand, the analytical implementation based on the local UC-DT (see Section II) is still very reliable, as confirmed by the full-wave simulations, at both micro- [see Fig. 10(c)–(d) versus Fig. 10(e)–(f)] and macro- [see Fig. 11(a)–(b) versus Fig. 11(c)–(d) and Fig. 12(a)–(b) versus Fig. 12(c)–(d)] scales. Moreover, the plots of the far-field reflection patterns in Fig. 11 point out, on the one hand, the challenging nature of the addressed shaped coverage SPSSs problems while, on the other hand, they prove the feasibility of SPSSs that focus selectively in narrow angular regions. The effectiveness of using an SPSS in an SEE context can be better appreciated when analyzing the footprint power densities (see Fig. 12). With reference to the HFSS simulations of the full-scale layouts, the reflected power is properly directed toward the user-defined coverage regions, regardless of their "dual beam" [see Fig. 12(a) and (c)] or "low grazing" [see Fig. 12(b) and (d)] nature, with limited power losses outside Θ (see Fig. 11). The quantitative assessment of such a behavior is given by the corresponding values of the efficiency index ζ_{HFSS}^{sha} ($\zeta^{sha} \triangleq (4\pi /)\Theta (\int_{\Theta} |\mathbf{F}(\mathbf{r}; \mathbf{G})|^2 r^2 \sin(\theta) \mathrm{d}\theta \mathrm{d}\varphi / \int_0^{2\pi} \int_0^{\pi} |\mathbf{F}(\mathbf{r}; \mathbf{G})|^2 r^2 \sin (\theta) \mathrm{d}\theta \mathrm{d}\varphi)$ being the average directivity in the footprint region for the SEE shaped coverage) being $\zeta_{HFSS}^{sha(Two-Squares)} = 18.81$ [dB] [see Fig. 12(c)] and $\zeta_{HFSS}^{sha(Street+Square)} = 20.92$ [dB] [see Fig. 12(d)].

The next example is aimed at answering to the following questions: "widening the aperture, the patterned surface similarity observed in the pencil coverage is still maintained when dealing with complex shaped footprints?" and "does the design rule $\delta\Xi \approx \delta\zeta$ apply also for complex shaped coverages?" Toward this end,

a $P \times Q = 75 \times 75$ square lattice comprising ≈ 5600 UCs with an extension of $\Xi \approx 3.2 \times 3.2$ [m^2] [see Fig. 13(a)] has been chosen to radiate the "street-square" footprint, and the performance of the arising layout has been compared with those of the smaller (i.e., $P \times Q = 50 \times 50$) arrangement in Fig. 10(b). By taking a look to the sketch of the SPSS in Fig. 13(a), the answer to the first question is that, unlike the pencil coverage case, the increase of the size seems to imply a "stretching" of the UCs distribution [see Figs. 13(a) versus 10(b)] rather than a "repetition" of the same spatial behavior [see Figs. 8(a) versus 5(a)] probably because of the need of affording more complex wave manipulation phenomena to generate the complex footprint at hand. As for the second question, let us compare the radiation behavior of the two SPSSs in Figs. 10(b) and 13(a) pictorially described by the footprint color maps in Figs. 12(d) and 13(b), respectively. Both layouts fulfill the requirement of reflecting the incident power toward the desired region Θ. This happens more and more as the SPSS support enlarges according to the rule-of-thumb $\delta\zeta^{sha} \approx \delta\Xi$. Indeed, $\delta\Xi \approx 3.5$ [dB] and $\delta\zeta_{HFSS}^{sha} \approx 3.2$ [dB] (i.e., $\zeta_{HFSS}^{sha}\rfloor_{P=Q=75} = 23.94$ [dB] [see Fig. 13(b)] and $\zeta_{HFSS}^{sha}\rfloor_{P=Q=50} = 20.92$ [dB] [see Fig. 12(d)]).

Whether the feasibility and the effectiveness of an SPSS deployment are key items to be addressed toward the implementation of an SEE, certainly the sustainable installation in a living environment (e.g., a town square of a city or a room in a building floor) is a relevant issue, as well. Without pretending to give "the" solution to this problem, but just for adding some insights on the topic, some tests in the underlying numerical analysis have been devoted to this line of reasoning. More specifically, a representative example dealt with the possibility to realize, on a standard "junior poster billboard" support [i.e., $\Xi \approx 3.6 \times 1.8$ [m^2]-Fig. 14(a)], an SPSS focusing the beam on the same "street-square" region Θ of the previous examples. Subject to the size constraint, the SPSS has been designed by optimizing the descriptors of $P \times Q = 84 \times 42$ UCs. Fig. 14 shows the synthesized layout [see Fig. 14(a)] along with the HFSS-simulated footprint pattern [see Fig. 14(b)]. As hoped, the radiated beam fulfills the mask requirements with a good accuracy being $\zeta_{HFSS}^{sha}\rfloor_{P \times Q=84 \times 42} = 21.30$ [dB] [see Fig. 14(b)], even though, unlike Fig. 13(b), some spill-over effects appear at low grazing angles (i.e., $y_{glob} > 140$ [m]) [see Fig. 14(b)] due to the smaller vertical size of the SPSS [see Figs. 14(a) versus 13(a)].

The last test case is not concerned with a realistic SEE problem, but it is more aimed at giving the flavor of what can be done with just a static and passive structure provided you have at disposal a suitable tool for managing the huge computational complexity of a high-dimension optimization problem. Accordingly, the proposed SPSS design has been applied to optimize a $P \times Q = 75 \times 75$ UCs arrangement, located $H = 20$ [m] on the floor, for beaming a "olympic flag"-shaped region of extension -150 [m] $\leq x_{glob} \leq 70$ [m] and 50 [m] $\leq y_{glob} \leq 150$ [m] (see Fig. 1). The plots of the synthesized layout [see Fig. 15(a)] and the HFSS-computed distribution of the power reflected on the ground [see Fig. 15(b)] prove the feasibility of an SPSS matching hard pattern-mask requirements
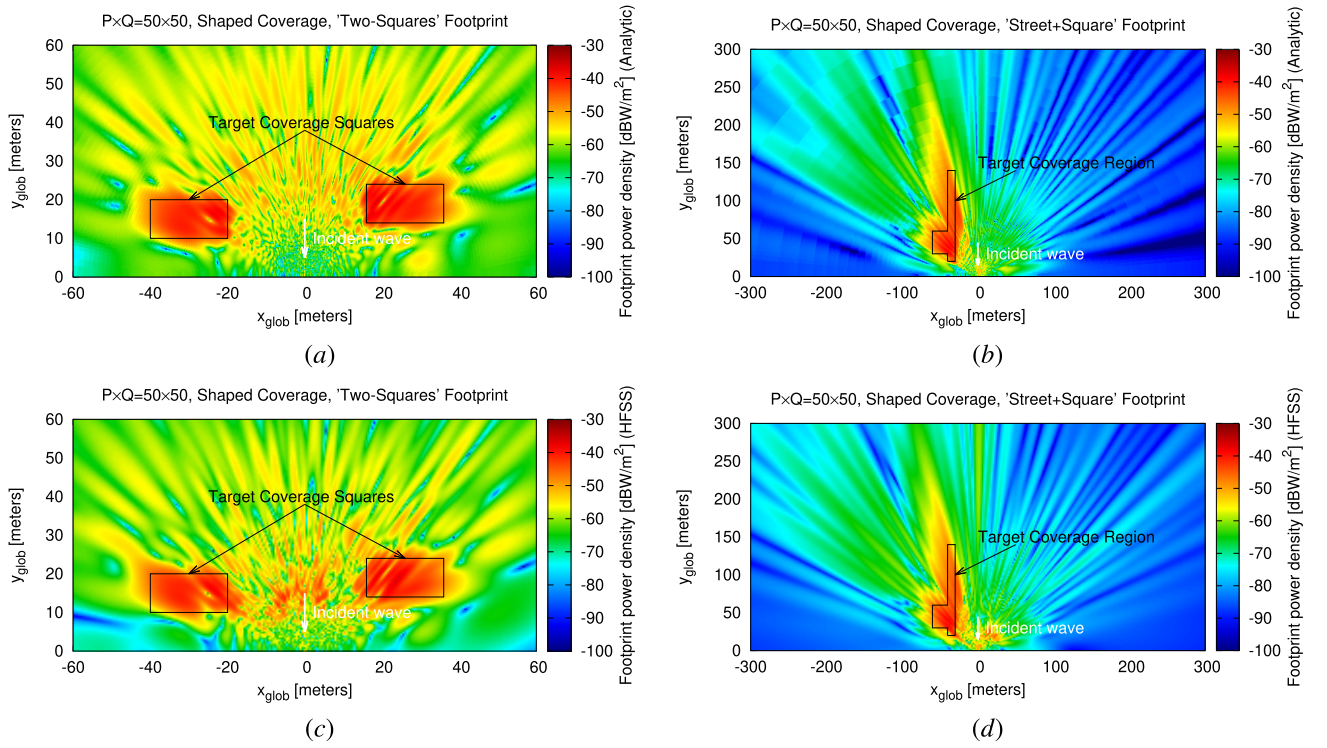
Fig. 12. Numerical validation (shaped coverage, $P = Q = 50$ and $H = 5$ [m])—(a) and (b) analytically computed and (c) and (d) HFSS-simulated SPSS footprint patterns in correspondence with (a) and (c) "two-square" and (b) and (d) "street-square" footprint targets.
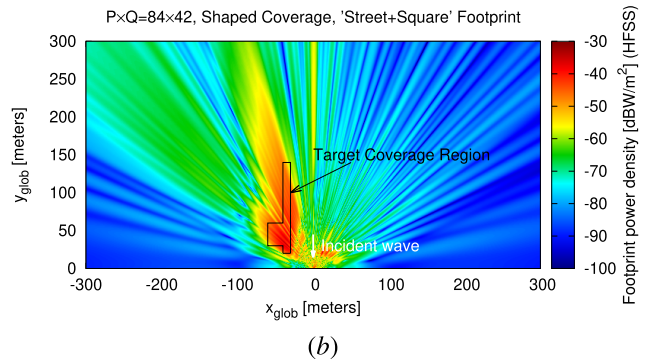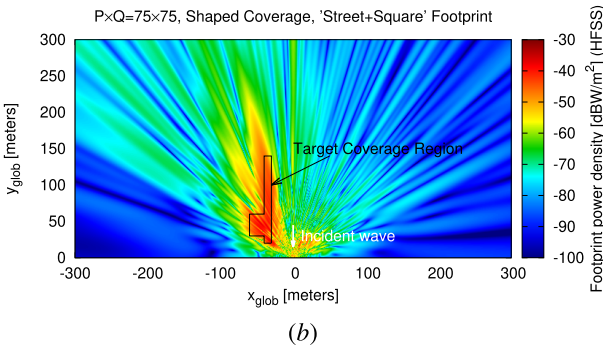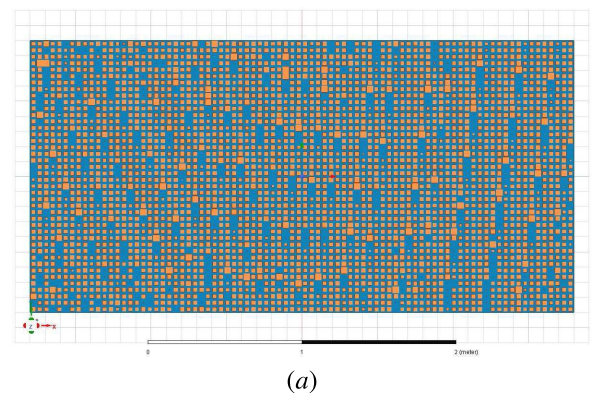

Fig. 13. Numerical validation (shaped coverage, "street-square" footprint, $P = Q = 75$ and $H = 5$ [m])—(a) synthesized SPSS layout and (b) HFSS-simulated SPSS footprint pattern.

Fig. 14. Numerical validation (shaped coverage, "street-square" footprint, $P \times Q = 84 \times 42$ and $H = 5$ [m])—(a) synthesized SPSS layout and (b) HFSS-simulated SPSS footprint pattern.

$[\varsigma_{HFSS}^{sha} \approx 18.3$ [dB]—Fig. 15(b)], as well as the capability of the proposed design method to efficiently deal with large-scale optimization problems.

For completeness, Table I provides the CPU time Δt for the online part of the design process [i.e., the IPT current computation (Δt^{IPT}) and the SbD layout optimization (Δt^{SbD})] for the
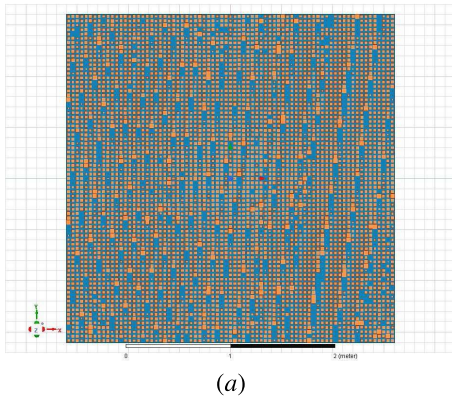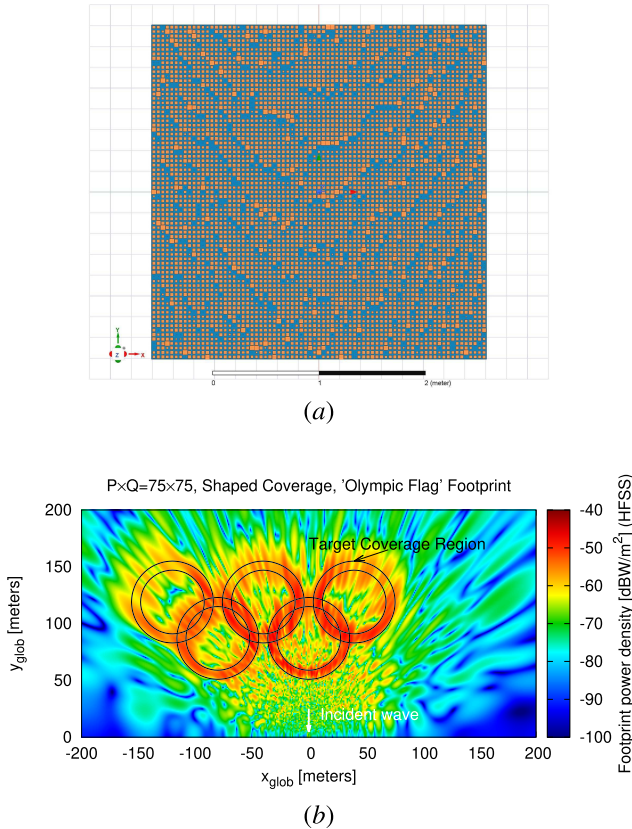
(a)

(b)

Fig. 15. Numerical validation (shaped coverage, "Olympic flag" footprint, $P = Q = 75$ and $H = 20$ [m])—(a) synthesized SPSS layout and (b) HFSS-simulated SPSS footprint pattern.

TABLE I
NUMERICAL VALIDATION. COMPUTATIONAL INDEXES

Design	Coverage	$P \times Q$	Δt^{IPT} [s]	Δt^{SbD} [s]
Fig. 5(a)	Pencil	30×30	1.31×10^2	2.52×10^{-1}
Fig. 8(a)	Pencil	50×50	1.46×10^2	6.15×10^{-1}
Fig. 10(a)	Two-Squares	50×50	1.46×10^2	6.35×10^{-1}
Fig. 10(b)	Street-Square	50×50	1.46×10^2	6.28×10^{-1}
Fig. 13(a)	Street-Square	75×75	1.50×10^2	1.16
Fig. 14(a)	Street-Square	84×42	1.50×10^2	1.16
Fig. 15(a)	Olympic Flag	75×75	1.52×10^2	1.22

previous case studies.[6] The reported results show that, likewise demonstrated in preliminary IPT-SbD implementations [11], the synthesis process turns out extremely fast (i.e., $\Delta t^{IPT} \leq 1.52 \times 10^2$ [s], $\Delta t^{SbD} \leq 1.22$ [s]—Table I) regardless of the coverage type (i.e., both "pencil" and "shaped" beams—Table I) and the SPSS aperture (i.e., $P \times Q \in [30 \times 30, 75 \times 75]$—Table I).

V. CONCLUSION

The feasibility of SPSSs with advanced wave manipulation properties has been addressed. A two-step design process, which combines the solution of an IS problem to determine the surface currents affording user-desired pattern-mask constraints together with an SbD-based optimization of the

---

[6]For the sake of fairness, all the computational times refer to a nonoptimized MATLAB implementation executed on a single-core laptop featuring a 1.60 GHz CPU clock. The time for the generation/training of the LSDDT block (Δt^{LSDDT}), which is equal to $\Delta t^{LSDDT} \approx 1.4 \times 10^4$ [s], is not included since it is performed only once and offline.

corresponding patterned layout, has been proposed. Toward this end, an innovative scheme for building an AI-based DT of the UCs of the SPSS for predicting the EM response of this latter has been introduced. The arising synthesis method has been validated by considering different apertures, radiation objectives, and various operative SEE scenarios. Full-wave finite element simulations [24] of the synthesized layouts have been performed to assess the reliability of the synthesis results.

The outcomes from the numerical validation have demonstrated that the proposed AI-driven method allows the designer to reliably synthesize large SPSSs with excellent beam control capabilities by efficiently solving high-dimension optimization problems. The exploitation of a Local UC-DT within the SbD-based optimization of the SPSS layout assures a faithful prediction of the EM behavior of the nonuniform modulated patterned surface while minimizing the computational costs of the solution of the forward problem at hand. The synthesis layouts fulfill challenging radiation objectives despite the choice of a basic UC with limited phase control.

Future works, beyond the scope of the present paper, will be aimed at exploring the potentialities of the proposed method when using more complex UCs (e.g., a higher number of per-element DoFs or multilayer structures) and tiled architectures instead of single-panel layouts. Moreover, the extension of the proposed method to real-time reconfigurable smart skins is currently under development.

APPENDIX

Small-Scale/Full-Scale Mapping Rules

The mapping rules between the predictions of the local surface susceptibility tensors of the small-scale SPSS, $\{\overline{\overline{\zeta}}_{p'q'}^{e/m}(\mathbf{G}'); p' = 1, \ldots, P'; q' = 1, \ldots, Q'\}$ and the predictions of the local surface susceptibility tensors of the full-scale SPSS, $\{\overline{\overline{\zeta}}_{pq}^{e/m}(\mathbf{G}); p = 1, \ldots, P; q = 1, \ldots, Q\}$, which estimates the corresponding actual values, $\{\overline{\overline{\psi}}_{pq}^{e/m}(\mathbf{G}); p = 1, \ldots, P; q = 1, \ldots, Q\}$, are defined as follows:

$$\overline{\overline{\zeta}}_{pq}^{e/m}(\mathbf{G}) = \begin{cases} \overline{\overline{\zeta}}_{p'q'}^{e/m}(\mathbf{G}') \Big]_{p'=p}^{q'=q} & if \ (p,q) \in \mathcal{C}^{(0)} \\ \overline{\overline{\zeta}}_{p'q'}^{e/m}(\mathbf{G}') \Big]_{p'=p-P+P'}^{q'=q-Q+Q'} & if \ (p,q) \in \mathcal{C}^{(1)} \\ \overline{\overline{\zeta}}_{p'q'}^{e/m}(\mathbf{G}') \Big]_{p'=p}^{q'=q-Q+Q'} & if \ (p,q) \in \mathcal{C}^{(2)} \\ \overline{\overline{\zeta}}_{p'q'}^{e/m}(\mathbf{G}') \Big]_{p'=p-P+P'}^{q'=q} & if \ (p,q) \in \mathcal{C}^{(3)} \\ \overline{\overline{\zeta}}_{p'q'}^{e/m}(\mathbf{G}') \Big]_{p'=p}^{q'=3} & if \ (p,q) \in \mathcal{C}^{(4)} \\ \overline{\overline{\zeta}}_{p'q'}^{e/m}(\mathbf{G}') \Big]_{p'=3}^{q'=q} & if \ (p,q) \in \mathcal{C}^{(5)} \\ \overline{\overline{\zeta}}_{p'q'}^{e/m}(\mathbf{G}') \Big]_{p'=3}^{q'=3} & if \ (p,q) \in \mathcal{C}^{(6)} \end{cases} \quad (17)$$

where $\mathcal{C}^{(0)} = \{(p,q) : p \in [1,2], q \in [1,2]\}$, $\mathcal{C}^{(1)} = \{(p,q) : p \in [P-1,P], q \in [Q-1,Q]\}$, $\mathcal{C}^{(2)} = \{(p,q) : p \in [1,2], q \in [Q-1,Q]\}$, $\mathcal{C}^{(3)} = \{(p,q) : p \in [P-1,P],$

$q \in [1, 2]\}$, $\mathcal{C}^{(4)} = \{(p, q) : p = \{1, 2, P - 1, P\}, q \in [3, Q - 2]\}$, $\mathcal{C}^{(5)} = \{(p, q) : p \in [3, P - 2], q = \{1, 2, Q - 1, Q\}\}$, and $\mathcal{C}^{(6)} = \{(p, q) : p \in [3, P - 2], q \in [3, Q - 2]\}$ (see Fig. 2).

ACKNOWLEDGMENT

REFERENCES

[1] E. Basar, M. Di Renzo, J. De Rosny, M. Debbah, M. Alouini, and R. Zhang, "Wireless communications through reconfigurable intelligent surfaces," *IEEE Access*, vol. 7, pp. 116753–116773, 2019.

[2] M. D. Renzo *et al.*, "Smart radio environments empowered by reconfigurable AI meta-surfaces: An idea whose time has come," *EURASIP J. Wireless Commun. Netw.*, vol. 2019, no. 1, pp. 1–20, Dec. 2019.

[3] M. Di Renzo *et al.*, "Smart radio environments empowered by reconfigurable intelligent surfaces: How it works, state of research, and the road ahead," *IEEE J. Sel. Areas Commun.*, vol. 38, no. 11, pp. 2450–2525, Nov. 2020.

[4] A. Massa and M. Salucci, "On the design of complex EM devices and systems through the system-by-design paradigm—A framework for dealing with the computational complexity," *IEEE Trans. Antennas Propag.*, vol. 70, no. 2, pp. 1328–1343, Feb. 2022.

[5] M. Di Renzo *et al.*, "Reconfigurable intelligent surfaces vs. relaying: Differences, similarities, and performance comparison," *IEEE Open J. Commun. Soc.*, vol. 1, pp. 798–807, 2020.

[6] W. Tang *et al.*, "Subject Editor spotlight on programmable metasurfaces: The future of wireless?" *IET Electron. Lett.*, vol. 55, no. 7, pp. 360–361, 2019.

[7] A. Massa *et al.*, "Designing smart electromagnetic environments for next-generation wireless communications," *Telecom*, vol. 2, no. 2, pp. 213–221, May 2021.

[8] A. Pitilakis *et al.*, "A multi-functional reconfigurable metasurface: Electromagnetic design accounting for fabrication aspects," *IEEE Trans. Antennas Propag.*, vol. 69, no. 3, pp. 1440–1454, Mar. 2021.

[9] C. Liaskos, S. Nie, A. Tsioliaridou, A. Pitsillides, S. Ioannidis, and I. Akyildiz, "A new wireless communication paradigm through software-controlled metasurfaces," *IEEE Commun. Mag.*, vol. 56, no. 9, pp. 162–169, Sep. 2018.

[10] C. Huang, A. Zappone, G. C. Alexandropoulos, M. Debbah, and C. Yuen, "Reconfigurable intelligent surfaces for energy efficiency in wireless communication," *IEEE Trans. Wireless Commun.*, vol. 18, no. 8, pp. 4157–4170, Aug. 2019.

[11] G. Oliveri, P. Rocca, M. Salucci, and A. Massa, "Holographic smart EM skins for advanced beam power shaping in next generation wireless environments," *IEEE J. Multiscale Multiphys. Comput. Techn.*, vol. 6, pp. 171–182, 2021.

[12] F. Yang and Y. Rahmat-Samii, *Surface Electromagnetics With Applications in Antenna, Microwave, and Optical Engineering*. Cambridge, U.K.: Cambridge Univ. Press, 2019.

[13] G. Oliveri, D. H. Werner, and A. Massa, "Reconfigurable electromagnetics through metamaterials—A review," *Proc. IEEE*, vol. 103, no. 7, pp. 1034–1056, Jul. 2015.

[14] G. Oliveri, F. Viani, N. Anselmi, and A. Massa, "Synthesis of multilayer WAIM coatings for planar-phased arrays within the system-by-design framework," *IEEE Trans. Antennas Propag.*, vol. 63, no. 6, pp. 2482–2496, Jun. 2015.

[15] G. Oliveri, A. Gelmini, A. Polo, N. Anselmi, and A. Massa, "System-by-design multiscale synthesis of task-oriented reflectarrays," *IEEE Trans. Antennas Propag.*, vol. 68, no. 4, pp. 2867–2882, Apr. 2020.

[16] A. Massa, G. Oliveri, P. Rocca, and F. Viani, "System-by-design: A new paradigm for handling design complexity," in *Proc. 8th Eur. Conf. Antennas Propag. (EuCAP)*, Apr. 2014, pp. 1180–1183.

[17] M. A. Ricoy and J. L. Volakis, "Derivation of generalized transition/boundary conditions for planar multiple-layer structures," *Radio Sci.*, vol. 25, no. 4, pp. 391–405, Jul./Aug. 1990.

[18] E. F. Kuester, M. A. Mohamed, M. Piket-May, and C. L. Holloway, "Averaged transition conditions for electromagnetic fields at a metafilm," *IEEE Trans. Antennas Propag.*, vol. 51, no. 10, pp. 2641–2651, Oct. 2003.

[19] K. Achouri, M. A. Salem, and C. Caloz, "General metasurface synthesis based on susceptibility tensors," *IEEE Trans. Antennas Propag.*, vol. 63, no. 7, pp. 2977–2991, Jul. 2015.

[20] P. Rocca, R. L. Haupt, and A. Massa, "Sidelobe reduction through element phase control in uniform subarrayed array antennas," *IEEE Antennas Wireless Propag. Lett.*, vol. 8, pp. 437–440, 2009.

[21] G. Oliveri, M. Salucci, N. Anselmi, and A. Massa, "Multiscale system-by-design synthesis of printed WAIMs for waveguide array enhancement," *IEEE J. Multiscale Multiphys. Comput. Tech.*, vol. 2, pp. 84–96, 2017.

[22] G. Oliveri, A. Polo, M. Salucci, G. Gottardi, and A. Massa, "*SbD*-based synthesis of low-profile *WAIM* superstrates for printed patch arrays," *IEEE Trans. Antennas Propag.*, vol. 69, no. 7, pp. 3849–3862, Jul. 2021.

[23] M. Salucci, L. Tenuti, G. Oliveri, and A. Massa, "Efficient prediction of the EM response of reflectarray antenna elements by an advanced statistical learning method," *IEEE Trans. Antennas Propag.*, vol. 66, no. 8, pp. 3995–4007, Aug. 2018.

[24] *ANSYS Electromagnetics Suite–HFSS*, ANSYS, Canonsburg, PA, USA, 2021.

[25] M. Salucci, A. Gelmini, G. Oliveri, N. Anselmi, and A. Massa, "Synthesis of shaped beam reflectarrays with constrained geometry by exploiting nonradiating surface currents," *IEEE Trans. Antennas Propag.*, vol. 66, no. 11, pp. 5805–5817, Nov. 2018.

[26] A. Osipov and S. Tretyakov, *Modern Electromagnetic Scattering Theory With Applications*. Hoboken, NJ, USA: Wiley, 2017.

[27] I. V. Lindell and A. Sihvola, *Boundary Conditions in Electromagnetics*. Piscataway, NJ, USA: IEEE Press, 2019.

[28] J. Huang and J. A. Encinar, *Reflectarray Antennas*. Hoboken, NJ, USA: Wiley, 2008.

[29] P. Rocca, M. Benedetti, M. Donelli, D. Franceschini, and A. Massa, "Evolutionary optimization as applied to inverse problems," *Inverse Problems*, vol. 25, pp. 1–41, Dec. 2009.

[30] M. Ciydem and E. A. Miran, "Dual-polarization wideband sub-6 GHz suspended patch antenna for 5G base station," *IEEE Antennas Wireless Propag. Lett.*, vol. 19, no. 7, pp. 1142–1146, Jul. 2020.

[31] G. Oliveri *et al.*, "Codesign of unconventional array architectures and antenna elements for 5G base stations," *IEEE Trans. Antennas Propag.*, vol. 65, no. 12, pp. 6752–6767, Dec. 2017.

Giacomo Oliveri (Senior Member, IEEE) received the B.S. and M.S. degrees in telecommunications engineering and the Ph.D. degree in space sciences and engineering from the University of Genoa, Genoa, Italy, in 2003, 2005, and 2009, respectively.

He was a Visiting Researcher at L2S in 2012, 2013, and 2015, an Invited Associate Professor at the University of Paris Sud, Paris, France, in 2014, and a Visiting Professor at Université Paris-Saclay in 2016 and 2017. He is currently an Associate Professor at the Department of Civil, Environmental and Mechanical Engineering, University of Trento, Trento, Italy, and a Board Member of the ELEDIA Research Center. Moreover, he is an Adjunct Professor at CentraleSupélec and a member of the Laboratoire des signaux et systèmes (L2S)@CentraleSupélec, Gif-sur-Yvette, France. He is the author/coauthor of over 400 peer-reviewed papers in international journals and conferences. His research work is mainly focused on electromagnetic direct and inverse problems, system-by-design and metamaterials, and antenna array synthesis.

Prof. Oliveri is the Chair of the IEEE AP/ED/MTT North Italy Chapter. He serves as an Associate Editor for the IEEE ANTENNAS AND WIRELESS PROPAGATION LETTERS, the IEEE JOURNAL ON MULTISCALE AND MULTIPHYSICS COMPUTATIONAL TECHNIQUES, *EPJ Applied Metamaterials*, the *International Journal of Antennas and Propagation*, the *International Journal of Distributed Sensor Networks*, the *Microwave Processing* journal, and the *Sensors* journal.

Francesco Zardi received the B.Sc. degree in telecommunications and electronic engineering and the M.Sc. degree in information and communications engineering from the University of Trento, Trento, Italy, in 2017 and 2019, respectively. He is currently pursuing the Ph.D. degree with the International Doctoral School in Information and Communication Technology of Trento.

He is a Senior Researcher with the ELEDIA Research Center. His research activity is mainly focused on advanced radar architectures and electromagnetic diagnostic techniques.

Paolo Rocca (Senior Member, IEEE) received the M.S. degree *(summa cum laude)* in telecommunications engineering and the Ph.D. degree in information and communication technologies from the University of Trento, Trento, Italy, in 2005 and 2008, respectively.

He has been a Visiting Ph.D. Student at Pennsylvania State University State College, PA, USA,, and the University Mediterranea of Reggio Calabria, Reggio Calabria, Italy, and a Visiting Researcher at the Laboratoire des Signaux et Systèmes (L2S@ Supèlec, Paris, France) in 2012 and 2013. Moreover, he has been an Invited Professor at the University of Paris Sud, Orsay, France, in 2015, and the University of Rennes 1, Rennes, France, in 2017. He is currently an Associate Professor at the Department of Civil, Environmental, and Mechanical Engineering, University of Trento, the Huashan Scholar Chair Professor at Xidian University, Xi'an, China, and a member of the ELEDIA Research CenterHe has authored or coauthored one book chapter, 150 journals, and more than 270 conference papers. His main interests are in the framework of artificial intelligence techniques as applied to electromagnetics, antenna array synthesis and analysis, and electromagnetic inverse scattering.

Prof. Rocca is a member of the Big Data and AI Working Group for the Committee on Engineering for Innovative Technologies (CEIT) of the World Federation of Engineering Organizations (WFEO). He received the National Scientific Qualification for the position of Full Professor in Italy and France in April 2017 and January 2020, respectively. He has been awarded from the IEEE Geoscience and Remote Sensing Society and the Italy Section with the Best PhD Thesis Award IEEE-GRS Central Italy Chapter. He served as an Associate Editor of the IEEE ANTENNAS AND WIRELESS PROPAGATION LETTERS from 2011 to 2016 and the *Microwave and Optical Technology Letters* from 2019 to 2020. He has been an Associate Editor of the *IEEE Antennas and Propagation Magazine* since 2020 and an Associate Editor of Engineering since 2020.

Marco Salucci (Senior Member, IEEE) received the M.S. degree in telecommunication engineering from the University of Trento, Trento, Italy, in 2011, and the Ph.D. degree from the International Doctoral School in Information and Communication Technology of Trento, Trento, Italy, in 2014.

He was a Post-Doctoral Researcher with CentraleSupélec, Paris, France, and the Commissariat à l'énergie atomique et aux énergies alternatives (CEA), Paris. He is currently a Researcher at the University of Trento and a member of the ELEDIA Research Center. His research activities are mainly concerned with inverse scattering, biomedical and GPR microwave imaging techniques, antenna synthesis, and computational electromagnetics with a focus on system-by-design methodologies integrating optimization techniques and learning-by-examples methods for real-world applications.

Dr. Salucci is a member of the IEEE Antennas and Propagation Society. He was also a member of the COST Action TU1208 "Civil Engineering Applications of Ground Penetrating Radar." He is also an Associate Editor for Communications and Memberships of the IEEE TRANSACTIONS ON ANTENNAS AND PROPAGATION. Moreover, he also serves as an Associate Editor of the IEEE TRANSACTIONS ON ANTENNAS AND PROPAGATION and a reviewer for different international journals, including IEEE TRANSACTIONS ON ANTENNAS AND PROPAGATION, IEEE ANTENNAS AND WIRELESS PROPAGATION LETTERS, IEEE JOURNAL ON MULTISCALE AND MULTI-PHYSICS COMPUTATIONAL TECHNIQUES, and *IET Microwaves, Antennas & Propagation*.

Andrea Massa (Fellow, IEEE) received the Laurea (M.S.) degree in electronic engineering and the Ph.D. degree in EECS from the University of Genoa, Genoa, Italy, in 1992 and 1996, respectively.

He is currently a Full Professor of electromagnetic fields at the University of Trento, where he currently teaches electromagnetic fields, inverse scattering techniques, antennas and wireless communications, wireless services and devices, and optimization techniques. He is also the Director of the Network of Federated Laboratories ELEDIA Research Center (www.eledia.org) located in Brunei, China, Czech, France, Greece, Italy, Japan, Perù, and Tunisia, with more than 150 researchers. Moreover, he is also a holder of a Chang-Jiang Chair Professorship with the University of Electronic Science and Technology of China (UESTC), Chengdu, China, a Professor with CentraleSupélec, Paris, France, and a Visiting Professor at Tsinghua University, Beijing, China. He has been a holder of the Senior DIGITEO Chair with L2S-CentraleSupélec and CEA LIST, Saclay, France, the UC3M-Santander Chair of Excellence with the Universidad Carlos III de Madrid, Madrid, Spain, an Adjunct Professor with Penn State University, State College, PA, USA, a Guest Professor with UESTC, and a Visiting Professor at the Missouri University of Science and Technology, Rolla, MO, USA, Nagasaki University, Nagasaki, Japan, the University of Paris Sud, Orsay, France, Kumamoto University, Kumamoto, Japan, and the National University of Singapore, Singapore. He has been appointed IEEE AP-S Distinguished Lecturer from 2016 to 2018. He has published more than 900 scientific publications among which more than 350 on international journals ($>13\,500$ citations—H-index $= 60$ [Scopus]; $>11\,000$ citations—H-index $= 54$ [ISI-WoS]; and $> 22\,000$ citations—H-index $= 87$ [Google Scholar]) and more than 550 in international conferences where he presented more than 200 invited contributions (>40 invited keynote speaker) (www.eledia.org/publications). He has organized more than 100 scientific sessions in international conferences and has participated in several technological projects in the national and international framework with both national agencies and companies (18 International PRJ, >5 M€; eight National PRJ, >5 M€; Ten Local PRJ, >2 M€; 63 Industrial PRJ, >10 M€; and six University PRJ, >300 K€). His research activities are mainly concerned with inverse problems, analysis/synthesis of antenna systems and large arrays, radar systems synthesis and signal processing, cross-layer optimization and planning of wireless/RF systems, semantic wireless technologies, system-by-design and material-by-design (metamaterials and reconfigurable-materials), and theory/applications of optimization techniques to engineering problems (telecommunications, medicine, and biology).

Prof. Massa is an IET Fellow and an Electromagnetic Academy Fellow. He is also a member of the Editorial Board of the *Journal of Electromagnetic Waves and Applications*, a Permanent Member of the "PIERS Technical Committee" and the "EuMW Technical Committee," and the ESoA member. He has been appointed to the Scientific Board of the "Società Italiana di Elettromagnetismo (SIEm)" and elected to the Scientific Board of the Interuniversity National Center for Telecommunications (CNIT). He has been appointed in 2011 by the National Agency for the Evaluation of the University System and National Research (ANVUR) as a member of the Recognized Expert Evaluation Group (Area 09, 'Industrial and Information Engineering') for the evaluation of the studies at the Italian University and Research Center for the period 2004–2010. Furthermore, he has been elected as the Italian Member of the Management Committee of the COST Action TU1208 "Civil Engineering Applications of Ground Penetrating Radar". He has served as an Associate Editor for the IEEE TRANSACTIONS ON ANTENNAS AND PROPAGATION from 2011 to 2014. He also serves as an Associate Editor for the *International Journal of Microwave and Wireless Technologies*.